

Negative quench induced excitation dynamics for ultracold bosons in one-dimensional lattices

S.I. Mistakidis,¹ L. Cao,^{1,2} and P. Schmelcher^{1,2}

¹*Zentrum für Optische Quantentechnologien, Universität Hamburg,*

Luruper Chaussee 149, 22761 Hamburg, Germany

²*The Hamburg Centre for Ultrafast Imaging, Universität Hamburg,*

Luruper Chaussee 149, 22761 Hamburg, Germany

(Dated: September 12, 2018)

Abstract

The nonequilibrium dynamics following a quench of strongly repulsive bosonic ensembles in one-dimensional finite lattices is investigated by employing interaction quenches and/or a ramp of the lattice potential. Both sudden and time-dependent quenches are analyzed in detail. For the case of interaction quenches we address the transition from the strong repulsive to the weakly-interacting regime, suppressing in this manner the heating of the system. The excitation modes such as the cradle process, the local breathing mode and the density-wave tunneling are examined via local density observables. In particular, the cradle mode is inherently related to the initial delocalization and, following a negative interaction quench, can be excited only for incommensurate setups with filling larger than unity. Complementary for setups with subunit filling the cradle mode is accessible with the aid of a negative quench of the lattice depth. Our results shed light on possible schemes to control the cradle and the breathing modes. Finally, employing the notion of fidelity we study the dynamical response of the system after a diabatic or adiabatic parameter modulation for short and long evolution times. The evolution of the system is obtained numerically using the ab-initio multi-layer multi-configuration time-dependent Hartree method for bosons which permits to follow non-equilibrium dynamics including the corresponding investigation of higher-band effects.

Keywords: sudden quench; time-dependent quench; interaction quench; barrier quench; non-equilibrium dynamics; controlled dynamics; higher-band effects; excitation modes; fidelity.

PACS numbers: 03.75.Lm, 67.57.Hi, 67.57.Jj, 67.85.-d, 67.85.Hj

I. INTRODUCTION

The realization of ultracold atomic gases has opened up exciting possibilities for the study of the non-equilibrium quantum dynamics of many-body systems [1, 2]. The high degree of tunability and the good isolation from the environment renders ultracold gases a versatile tool to realize systems far from equilibrium as they remain coherent for sufficiently long time scales, allowing us to probe them experimentally. In particular, the dynamical response of a closed quantum system can be investigated via a sudden change (i.e. a rapid perturbation compared to any other characteristic time scale of the system) of a Hamiltonian parameter called 'quantum quench'. Typically, in such a scenario the many-body system is initially prepared in a characteristic state which is not an eigenstate of the perturbed Hamiltonian, and the subsequent time-evolution is explored. In this way, important aspects can be studied such as the connection between the final and initial states or the emergence of a steady state [3]. Despite recent theoretical advances (see Ref. [2] and references therein), our understanding of strongly correlated quantum gases after a quench is far from complete and constitutes an appealing problem of modern quantum physics.

From the experimental viewpoint using either optical or magnetic Feshbach resonances [4–7] one can increase the strength of the interparticle interaction almost arbitrarily. In turn, strong interactions in optical lattices can cause substantial excited-band populations which render the lowest-band approximation inadequate for a quantitative or even qualitative description of the dynamics. In this direction, recent experiments have investigated multiorbital dynamics [8], unconventional superfluidity [9, 10] and the orbital excitation blockade [11]. On the theoretical side, the formation of supersolid quantum phases in cubic lattices [12], antiferromagnetic ordering of orbital angular momentum [13, 14], quantum stripe ordering in triangular lattices [15] and Wigner crystallization in honeycomb lattices [16] have been explored.

Alternatively, one can start from strong interactions and quench back to the weakly interacting region. This scenario has been used to study the light-cone spreading of correlations [17, 18], the question of thermalization [3, 19] and the Kibble-Zurek mechanism [20, 21] to name only a few. Further phenomena arising from strongly correlated quenched ensembles have revealed the pinning transition [22], the occurrence of collapse and revival oscillations of matter-wave phase coherence [23] and Anderson's orthogonality catastrophe for a mixture consisting of a Tonks pair and a single impurity [24].

Most of the above topics have been treated within mean field theory which serves as a convenient tool to deal with many-body phenomena, but can not capture important aspects of the emergent

strongly correlated physics. From the experimental perspective however the arising fluctuations can now be studied in the framework of ultracold gases due to recent advances [25–27]. A common technique to probe these fluctuations is the addition of optical lattices, which permits the study of the trap-related excited modes beyond the mean field regime. Here, important on-site energetically lowest normal modes are the breathing (or monopole) mode [28–33] and the dipole (or sloshing) mode [34, 35]. In particular, these modes can also be revealed during the dynamics following a quantum quench. In a previous work [36] we explored the dynamics of positive interaction quenched superfluids, where we detected a cradle and a local-breathing mode as well as the occurrence of a resonance between a tunneling mode and the cradle. However, starting from strong interactions and performing a negative quench may lead to a drastically different dynamical behaviour as the filling factor ν is expected to play a crucial role. Here, an intriguing aspect would be to explore how the initial spatial configuration of the system, reflected by the corresponding filling factor, affects the system dynamics and as a consequence the generation of the emergent excited modes. This investigation will permit us to gain a deeper understanding of the on-site excited modes (especially the cradle mode), the underlying microscopic mechanisms and their controllability in terms of the tunable parameters of the Hamiltonian. Note also that for such a scenario one can minimize heating processes [37], i.e. avoid particle losses from the optical trap.

In this work a systematic ab-initio analysis of the non-equilibrium dynamics of strongly repulsive interacting bosons in one-dimensional lattices is carried out. To this end, we study from a few-body perspective the dynamical effects resulting from an abrupt quench or time-dependent modulation of a Hamiltonian parameter, focussing on the few-body collective excitations and the control of the dynamics. In particular, we start from strong repulsive interactions and perform negative quenches either on the interparticle repulsion or on the optical lattice depth. This permits us to unravel the transport properties and the emergent excitation modes i.e. the local breathing and the cradle processes. Especially, for the case of a negative interaction quench we demonstrate that the cradle mode can be excited only for incommensurate setups with filling factor $\nu > 1$, exploiting the initial delocalization. On the other hand, for filling $\nu < 1$ in order to access this mode we use as a tool a barrier quench, thereby enforcing the over-barrier transport which in turn can generate the cradle mode. We show the persistence of the dynamical modes for finite-ramp rates and long evolution times accessible in recent experiments. The concept of fidelity is extensively applied in order to study the response of the quenched system and the transition from the diabatic to the adiabatic limit. The dynamical evolution is analyzed by employing the corresponding one-body densities and their fluctuations shedding light on the inter and intra well dynamics. Fourier spectra of local

density observables are used to give insight into the dynamical modes and their controllability upon the variation of a Hamiltonian parameter. The resulting non-perturbative dynamics (large quench) is explored using the recently developed numerically exact multi-layer multi-configuration time-dependent Hartree method for bosons [38, 39] (ML-MCTDHB) which reduces in our case of a single species to MCTDHB [40, 41].

This article is organized as follows. In Sec.II we explain the setup, the basic observables, as well as the general quench scenario and the representation of the wavefunction. Sec.III is devoted to a detailed study of the non-equilibrium quantum dynamics for two different quench protocols for incommensurable setups. We summarize and give an outlook in Sec.IV. Our computational method ML-MCTDHB is described in the Appendix.

II. THEORETICAL FRAMEWORK

A. The Hamiltonian

We investigate the strongly correlated non-equilibrium quantum dynamics of ultracold few-body systems confined in one-dimensional n -well optical lattices with N identical bosons of mass m . The corresponding dynamics is induced by the modulation of a parameter. The many-body Hamiltonian reads

$$H = \sum_{i=1}^N -\frac{\hbar^2}{2m} \frac{\partial^2}{\partial x_i^2} + V_{tr}(x_i) + \sum_{i<j} V_{int}(x_i - x_j). \quad (1)$$

Here, the short-range contact interaction potential $V_{int}(x_i - x_j) = g_{1D}\delta(x_i - x_j)$ between particles located at positions x_i , $i = 1, 2, \dots, N$ is represented by a Dirac delta-function. The interaction is well described by s-wave scattering and the effective 1D coupling strength [4] becomes $g_{1D} = \frac{2\hbar^2 a_0}{ma_{\perp}^2} \left(1 - \frac{|\zeta(1/2)|a_0}{\sqrt{2}a_{\perp}}\right)^{-1}$. The transversal length scale is $a_{\perp} = \sqrt{\frac{\hbar}{m\omega_{\perp}}}$, with ω_{\perp} the frequency of the confinement, whereas a_0 denotes the 3D s-wave scattering length. Therefore, the interaction strength can be tuned either via a_0 with the aid of a Feshbach resonance [7], or the transversal confinement frequency ω_{\perp} [4, 42, 44]. We model the 1D lattice potential as $V_{tr}(x_i) = V_0 \sin^2(kx_i)$, which is characterized by the barrier height V_0 and a periodicity $k = \frac{\pi}{l}$, where l denotes the distance between two successive potential minima. For our simulations we have used a sufficiently large lattice depth $V_0 = 6.0$ which is of the order of 3.0 to 4.0 E_R (depending on k), such that each well contains at least two localized single-particle Wannier states. Furthermore, in order to confine the bosons in the n -well system, we impose hard-wall boundary conditions at the appropriate position $x = \pm \frac{n\pi}{2k}$. In the following, for reasons of universality as well as of computational convenience we

shall use dimensionless units. To this end, the Hamiltonian (1) is rescaled in units of the recoil energy $E_r = \frac{\hbar^2 k^2}{2m}$. Thus, the spatial and temporal coordinates are given in units of k^{-1} and $\hbar E_r^{-1}$ respectively. Additionally, we set $\hbar = m = k = 1$ and the coupling strength becomes $g = g_{1D}/E_r$, while e.g. for a triple-well potential we have $V_{tr}(x) = V_0 \sin^2(x)$ with the hard wall boundaries located at the positions $x = \pm 3\pi/2$.

B. Observables

Using ML-MCTDHB the complete N -particle bosonic wave-function is available for every time step during the evolution. It is however desirable to extract the relevant information and (reduced) observables, in particular those related to experimentally accessible observables [1, 45]. In this respect, a straightforward measure is the single particle density

$$\rho(x, t) = \int dx_2 \dots dx_N |\Psi(x, x_2, \dots, x_N; t)|^2, \quad (2)$$

which is connected to the number density $n(x, t) = N\rho(x, t)$. Furthermore, in order to unravel the inner-well dynamics we extract the background by defining the deviation of the instantaneous density from the average value up to time T as $\delta\rho(x, t) = \rho(x, t) - \langle\rho(x)\rangle_T$. Here, the term $\langle\rho(x)\rangle_T = (1/T) \int_0^T dt \rho(x, t)$ corresponds to the mean single-particle probability density in the respective position during the dynamics. In this manner, we shall treat $\langle\rho(x)\rangle_T$ as the "macroscopic" component of the one-body density while $\delta\rho(x, t)$ constitutes the respective fluctuations.

An additional useful quantity is the one-body reduced density matrix

$$\rho^{(1)}(x, x'; t) = N \int dx_1 \dots dx_{N-1} \Psi(x, x_1, \dots, x_{N-1}; t) \Psi^*(x', x_1, \dots, x_{N-1}; t), \quad (3)$$

with N a normalization factor. From here it is obvious that the diagonal elements $\rho^{(1)}(x, x; t)$ of this matrix correspond to the known density of a certain region in the lattice while the off-diagonal $\rho^{(1)}(x, x'; t)$ parts can be used as a measure of the coherence as they indicate off-diagonal long range order in an infinite lattice. However, for our finite setups we can not conclude true off-diagonal long range order and this term refers to the appearance of short and long range one-body correlations. Furthermore, an expansion in terms of its eigenfunctions (the natural orbitals $\varphi_\alpha(x, t)$) leads to the following spectral decomposition

$$\rho^{(1)}(x, x'; t) = \sum_a n_a(t) \varphi_\alpha(x, t) \varphi_\alpha^*(x', t), \quad (4)$$

where $n_a \in [0, 1]$ is the population of the corresponding natural orbital φ_α . In turn the eigenvalues $n_a(t)$ can be used to characterize the system as condensed or fragmented [46–49]. Thus, if there

is only one non-zero macroscopically occupied eigenvalue n_0 the system is said to be condensed, otherwise fragmented.

C. The general quench concept

Let us consider a Hamiltonian that depends on k parameters, i.e. $H(\lambda_1, \lambda_2, \dots, \lambda_k)$. The system is supposed to be initially ($t = 0$) in the ground state $|\Psi(0)\rangle$ of the Hamiltonian $H_{in} = H(\lambda_{1;in}, \lambda_{2;in}, \dots, \lambda_{k;in})$, where $\lambda_{i;in}$ is some initial value of the parameter λ_i of the system associated to the perturber (see below). This can be for instance the interatomic interaction strength, the optical potential depth, the frequency of the lattice potential etc. Then, in order to explore the dynamical response of the system we change a set of these parameters according to the desired scheme. For simplicity here, we assume a change in only one parameter and let the system evolve under the new Hamiltonian $H_f = H(\lambda_{1;in}, \dots, \lambda_{i;f}, \dots, \lambda_{k;in})$. Note that the modulation of the parameter can be performed either abruptly or as a function of time $\lambda_{i;f} = g(\lambda_{i;in}; t)$. Therefore, the final Hamiltonian may depend explicitly on time t , while is chosen in our case to be linear $H_f(\lambda; t) = H_{in}(\lambda_{in}; t) + \lambda H_r$. The term H_r is a dimensionless perturbing operator due to scaling and λ , which has energy dimensions is the quench amplitude. The dynamical evolution is incorporated into the time-evolution operator

$$U_\lambda(t) = \hat{T} \exp \left(-\frac{i}{\hbar} \int_0^t dt' H_f(\lambda; t') \right), \quad (5)$$

where \hat{T} denotes the time ordering and the time-evolved state is given by $|\Psi_\lambda(t)\rangle = U_\lambda(t) |\Psi(0)\rangle$. However, when the system is subjected to a perturbation one naturally tries to measure the sensitivity of the quantum state. To quantify this sensitivity we employ the fidelity $F_\lambda(t)$ or Loschmidt echo [50], which is the absolute square of the overlap between states evolved under the unperturbed Hamiltonian and states evolved by the perturbed Hamiltonian i.e.

$$F_\lambda(t) = |f_\lambda(t)|^2, \quad (6)$$

with $f_\lambda(t) = \langle \Psi(0) | U_0(-t) U_\lambda(t) | \Psi(0) \rangle = \langle \Psi_0(t) | \Psi_\lambda(t) \rangle$.

D. Wavefunction representation

We describe the expansion of the wavefunction in terms of a multiband Wannier number state representation that inherently includes the information of excited bands. Such an expansion can

be proven very convenient when one deals with lattice systems and can appropriately describe phenomena in which the spatial localization of states plays a significant role covering intraband and interband processes.

We introduce a generalized number state representation in terms of the number states of non-interacting bosons which is also valid in the strong interaction regime if the number of the supplied single-particle functions is sufficient. Let us consider a lattice system consisting of N bosons and n -wells. Then, the bosonic wavefunction in terms of the aforementioned states, reads

$$|\Psi\rangle = \sum_{N,I} C_{N,I} |N_1, N_2, \dots, N_n\rangle_I. \quad (7)$$

Here, the summation runs over the different distributions of the $N = \sum_i N_i$ bosons and the respective possible excited states, denoted by the index I , that we must take into account according to their energetical order. In order to illustrate the utility of the method let us elaborate the corresponding number states for a system consisting of four bosons ($N=4$) in a triple-well ($n=3$) whose dynamics will be explored later on. Here, we can realize four different categories of number states. The quadruple mode $\{|4, 0, 0\rangle_I, |0, 4, 0\rangle_I, |0, 0, 4\rangle_I\}$ refers to four bosons in the same well, whereas the triple mode $\{|3, 1, 0\rangle_I, |0, 3, 1\rangle_I, |1, 0, 3\rangle_I, |1, 3, 0\rangle_I, |0, 1, 3\rangle_I, |3, 0, 1\rangle_I\}$ implies that three bosons are localized in the same well and the fourth resides in another well. On the other hand, the pair mode can be separated into two categories, the double pair mode $\{|2, 2, 0\rangle_I, |0, 2, 2\rangle_I, |2, 0, 2\rangle_I\}$ where the bosons are divided into two pairs with each of them in a different well and the single pair mode $\{|2, 1, 1\rangle_I, |1, 2, 1\rangle_I, |1, 1, 2\rangle_I\}$ that contains a pair and two separated bosons. For a conceptual understanding of the above notation we present in Table I the energetic decomposition of some in the following analysis frequently used number states. Within this representation we map the global notation of the energetical order (index I) to a detailed decomposition of number states that refer to each energetical level (superscript in each element).

Finally, due to their significance concerning the explanation of various aspects of the out-of-equilibrium dynamics, we make here a link between the categories of number states and the eigenstates of the system. The number states of a particular category with the same intrawell energetical index I share a similar on-site energy and they will significantly contribute to the same eigenstates. As a consequence the eigenstates can be also classified with respect to the dominantly contributing number states, e.g. the single-pair (SP), the double-pair (DP), the triple (T) and the quadruple (Q) mode. Thus, in the following we adapt the more compact notation $|\zeta\rangle_{\alpha,I}$ for the characterization of the eigenstates in terms of the number states. Here, the index α refers to the spatial occupation, i.e. it holds $\alpha = 1$ for the SP, $\alpha = 2$ for the DP etc whereas the

TABLE I. Energetic decomposition of some frequently used number states. The index I refers to the energetical order and is used as a compact notation instead of the detailed decomposition. Note that in the decomposition each element N^i refers to the i -th energetical level (superscript) of N non-interacting bosons in a particular well.

index I	$ 2, 1, 1\rangle_I$	$ 1, 2, 1\rangle_I$
$I = 0$	$ 2^0, 1^0, 1^0\rangle$	$ 1^0, 2^0, 1^0\rangle$
$I = 1$	$ 1^0 \otimes 1^1, 1^0, 1^0\rangle$	$ 1^1, 2^0, 1^0\rangle$
$I = 2$	$ 2^0, 1^1, 1^0\rangle$	$ 1^0, 1^0 \otimes 1^1, 1^0\rangle$
$I = 3$	$ 2^0, 1^0, 1^2\rangle$	$ 1^0, 2^0, 1^1\rangle$
$I = 4$	$ 1^1 \otimes 1^2, 1^0, 1^0\rangle$	$ 1^2, 2^0, 1^0\rangle$
$I = 5$	$ 2^0, 1^2, 1^0\rangle$	$ 1^0, 1^0 \otimes 1^2, 1^0\rangle$

index I denotes the respective energetical level and ζ stands for the index within each group. For instance $\{|\zeta\rangle_{3;1}\}$ represent the eigenstates which are dominated by the set of the triple states $\{|3, 1, 0\rangle_1, |0, 3, 1\rangle_1, |1, 0, 3\rangle_1, |1, 3, 0\rangle_1, |0, 1, 3\rangle_1, |3, 0, 1\rangle_1\}$, and the index ζ runs from 1 to 6.

III. QUENCH DYNAMICS

Before exploring the dynamics, some remarks concerning the ground states in the lattice for different particle numbers are in order. For lattice systems the role of commensurability is very important as one can realize two main categories with respect to the filling factor $\nu = N/n$, where N denotes the particle number and n the number of the wells. The commensurate case ($\nu = 1, 2, \dots$) is characterized by a proportionality between the number of particles and the wells while for an incommensurate case the filling is a noninteger number. In the first case, concerning the ground state it is known that for increasing interparticle interaction one can realize the superfluid to Mott insulator phase transition [51] which has been addressed extensively in the past years. On the other hand, for a system with an incommensurate filling $\nu \neq 1, 2, \dots$ the main feature is the existence of a delocalized fraction of particles which forbids the occurrence of a Mott state. Here, one can distinguish two physical situations: (a) the case $\nu > 1$ where on-site interaction effects prevail and (b) $\nu < 1$ in which the main concern is the redistribution of the particles over the sites as the interaction increases. This delocalized phase can also be explained in terms of the particle hole states using a strong coupling expansion [52, 53]. Indeed, for a Mott ground state, if we assume a non-zero tunneling energy (which is small compared to the interparticle interaction) using perturbation theory with respect to the tunneling operator one can prove that to zeroth order

the Mott state is given by $|\Psi_{Mott}(N_0)\rangle^{(0)} = \prod_{i=1}^n \left(\frac{1}{\sqrt{N_0!}} (a_i^\dagger)^{N_0} |0\rangle \right)$. Here, n denotes the number of sites, N_0 the number of bosons on each site, a_i^\dagger the creation operator acting on site i and $|0\rangle$ the vacuum state. The state of an incommensurate setup can be obtained as a correction of this wavefunction simply by annihilating (creating) $n - N$ particles from the Mott state [52, 53].

In the present study we consider the quench dynamics for setups with site occupancy different from unity and therefore exclude the Mott state physics. We proceed with a short reference to the ground state and consequently analyze the dynamical process following each quench protocol.

A. Quench from strong to weak interactions for filling $\nu > 1$

In this section, we focus on a system consisting of four strongly interacting bosons in a triple-well, i.e. with filling $\nu > 1$. The initial state before the quench is characterized by the competition between delocalization and on-site interaction effects. For strong interparticle repulsion, as we consider here ($g = 5.0$), this state can be interpreted as a fraction $N \bmod n$ of extra delocalized particles being on a commensurate background of localized particles. On the one-body level the on-site populations are quite similar which can be attributed to the localized background, while their slight discrepancy is due to the non-uniform distribution of the extra particle in the first excited band. The latter prevents the formation of a perfect insulator phase even for strong repulsion. Our goal is to investigate the dynamical processes following a negative quench of the interaction strength, thereby approaching the weakly interacting regime. For a quench protocol (see also Sec. II-C) the final Hamiltonian H_f can be constructed as a sum of a part H_0 which provides the pre-quenched state of the system and an additional part that denotes the perturbation

$$H_f(g_f, V) = H_0(g_{in}, V) + \frac{\delta g}{g_{in}} \sum_{k < j} V_{in}(x_k - x_j), \quad (8)$$

where g_{in} and g_f are the initial and final interaction strengths respectively, and $\delta g = g_f - g_{in}$ is the quench amplitude focussing here on $\delta g < 0$ and $\left| \frac{\delta g}{g_{in}} \right| \sim 1$.

In the following subsections we first proceed with a brief fragmentation analysis inspired from the perspective of natural orbitals in order to analyze the peculiarities of a negative interaction quench. Then we explain in some detail the response of the system in terms of the density-wave tunneling related to the dynamical transport and investigate each of the emergent excited normal modes consisting of a local breathing mode in the central well and a dipole-like cradle mode in the outer wells. A study for the manipulation of the excited modes is also provided. Finally, an investigation of the presence of the aforementioned modes for the case of a finite ramp follows.

1. Dynamical fragmentation

In this subsection, we analyze the role of dynamical fragmentation, i.e. the occurrence of more than one significantly occupied quantum states during the evolution, with a varying quench amplitude. Especially, the fragmentation in the non-equilibrium dynamics of trapped finite systems is known to depend strongly on the particle number [48, 54], the interaction strength and the evolution time. The spectral decomposition of the one-body reduced density matrix offers a measure of fragmentation via the populations $n_a(t)$ of the natural orbitals $\phi_a(t)$ (see eq.(4)). In particular, a non-fragmented (condensed) state requires the occupation of $n_0(t)$ to be close to unity [49].

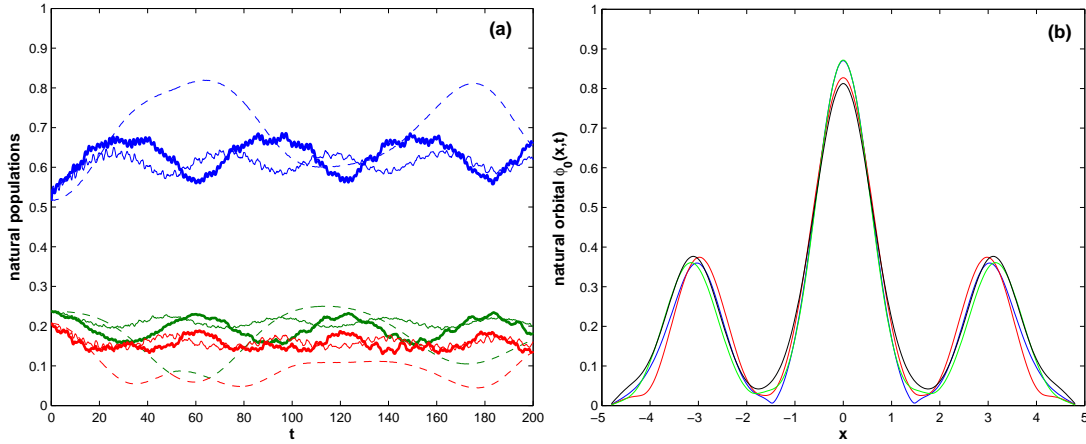


FIG. 1. Fragmentation analysis for a system of four bosons in a triple-well with $g_{in} = 5.0$. Shown are (a) the time evolution of the first three occupations $n_0(t)$ (blue lines), $n_1(t)$ (green lines), $n_2(t)$ (red lines) for different quench amplitudes $\delta g = -4.9$ (dashed lines), $\delta g = -4.0$ (thick solid lines) and $\delta g = -2.5$ (thin solid lines). (b) Profiles of the lowest natural orbital for a quench amplitude $\delta g = -4.95$ and different time instants during the evolution $t_1 = 0.9$ (blue), $t_2 = 2.6$ (red), $t_3 = 4.0$ (light-green) and $t_4 = 7.0$ (black).

Figure 1(a) shows the evolution of the first three natural populations for different quench amplitudes. The population of the first orbital $n_0(t)$ is always significantly below unity which confirms the fragmentation process, while the first three orbitals add up to more than 90% of the population. Focussing on the first orbital we note that the fragmentation is enhanced for quenches within the strong interaction regime and reduced when we quench to weak interactions. Especially, for final interactions close to a non-interacting state we observe a tendency for a non-fragmented state at least for certain time periods. This constitutes a major difference between a negative and a positive interaction quench scenario. In the latter case the fragmentation process is enhanced for larger quench amplitudes which can be attributed to the consequent raise of two-body correlations

during the process. However, here we face the inverse behaviour because in the initial strongly interacting state the two-body terms possess already a significant contribution which tend to be reduced after the quench. The above remarks can also lead us to the conclusion that the rate at which the two-body correlations are turned-off when we quench from strong-to-weak interactions is much smaller than the rate in which the two-body terms raises for a quench scenario from weak-to-strong interactions. Moreover, the second and third orbitals take on a compensatory role to the first, e.g. in the time periods where $n_0(t)$ is enhanced $n_1(t)$ and $n_2(t)$ are reduced. Finally, note that for smaller quenches the latter populations possess smaller amplitude oscillations whereas strong quenches introduce large amplitude variations of the populations. The observed oscillatory behaviour even for long times is a consequence of the finite size of the system.

Figure 1(b) illustrates the response of the first natural orbital $\phi_0(x, t)$ at different time-instants during the evolution after a quench to $g_f = 0.05$. As it can be seen $\phi_0(x, t)$ exhibits spatial oscillations in the outer wells and an on-site broadening in the middle well which accounts for interaction effects. Another important remark is that the band-structure is effectively reflected by the population of the natural orbitals, i.e. the orbitals $\phi_0(x)$, $\phi_1(x)$ and $\phi_2(x)$ correspond to the effective first band, orbitals $\phi_3(x)$, $\phi_4(x)$ and $\phi_5(x)$ to the second band etc. Thus, the lowest orbital $\phi_0(x, t)$ follows quite well the evolution of the quenched one-body density which will be discussed below (see also Figure 2).

2. Dynamical response and transport properties

We now study the tunneling dynamics, induced by a negative interaction quench first focussing on the single particle properties. Figure 2 illustrates the evolution of the one-body density following quenches for the weak interaction regime with $g_f = 0.02$ (Figure 2(a)) and the intermediate one with $g_f = 2.0$ (Figure 2(b)). We observe oscillations of the density in every site caused by the interaction quench which changes the repulsion among the bosons and as a consequence the time scales of the on-site oscillations. For $g_f = 2.0$ the quench has a less pronounced impact on the density profiles leading predominantly to a periodical squeezing of the density of the middle well during the evolution. Increasing δg this behaviour is enhanced and the atoms redistribute among the wells in a more prominent way spending also more time in the outer wells. The spatial oscillations of the one-body density are manifested as density-waves and reflect the transport properties in the system. This process of density-wave tunneling is more prominent when approaching a non-interacting system. It reflects the dynamical tunneling by changing its shape during the dynamics

from a dip-crest-dip to a crest-dip-crest spatial configuration (see also Figure 6).

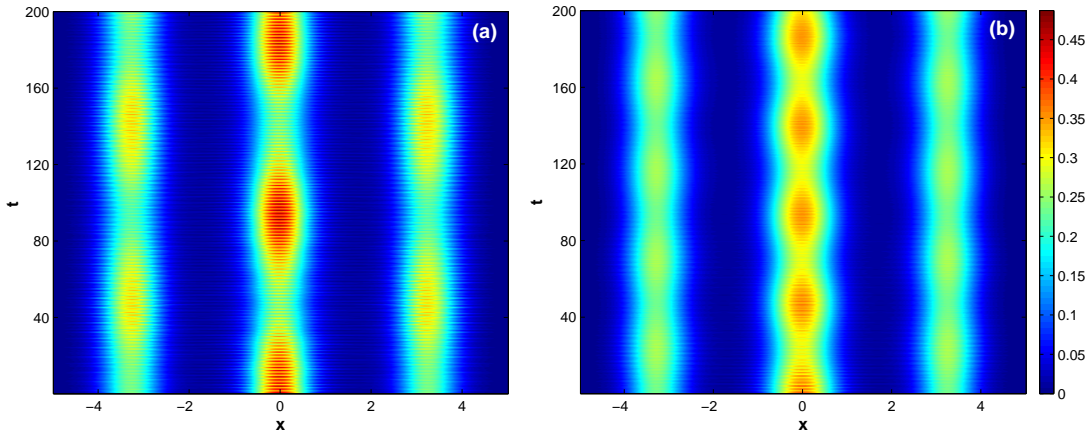


FIG. 2. One-body density $\rho(x, t)$ induced by quenches a) to weak interactions $g_f = 0.02$ and b) to intermediate interactions with $g_f = 2.0$. The initial state corresponds to the ground state of $N=4$ bosons confined in a triple-well in the strong interacting regime for $g_{in} = 5.0$.

In order to investigate further the dynamical response of the system we use the above-discussed fidelity $F_\lambda(t)$ (see eq.(6)). This quantity is shown in Figure 3(a) as a function of the final interaction strength and the time. We mainly note the appearance of two different regions as a function of the quench amplitude. The first one corresponds to quenches from a strong repulsive state with $g_{in} = 5.0$ to intermediate interactions where $3.4 < g_f < 5.0$. Here, the overlap during the dynamics is rather large with minimal percentage up to 85% and therefore the system is quite insensitive to the quench. In the second region where the final state belongs to weak or even to the non-interacting regime, i.e. $0 < g_f < 3.4$, we observe the formation of an oscillatory pattern in the fidelity evolution. This pattern indicates the sensitivity of the system to these type of quenches meaning that the system can be driven far from the initial state, while the minimal overlap for the extreme case of $g_f \rightarrow 0$ can even be of the order of 20%. The emergence of the above regions is universal in the system in the sense that it weakly depends on the height of the barrier. Thus, for an increasing barrier height the second region (larger quenches) will become narrower due to the larger potential energy which inhibits a possible departure of the system from the initial state.

In order to identify the tunneling modes participating in the dynamics we use as a measure the spectrum of the fidelity $F_\lambda(\omega) = \frac{1}{\pi} \int dt F_\lambda(t) e^{i\omega t}$. Indeed, Figure 3(b) shows $F_\lambda(\omega)$ for four different final interactions where we observe two dominant tunneling peaks. To proceed with a more quantitative description of the tunneling dynamics we shall expand the wavefunction in

terms of the number states introduced in Section II-D. To this end, let $|\Psi(0)\rangle = \sum_{\zeta;\alpha;I} C_{\zeta}^{\alpha;I} |\zeta\rangle_{\alpha;I}$ be the initial wavefunction in terms of the eigenstates $|\zeta\rangle_{\alpha;I}$ of the final Hamiltonian. Then, the expansion of the fidelity reads

$$|\langle\Psi(0)|\Psi(t)\rangle|^2 = \sum_{\zeta_1;\alpha;I} |C_{\zeta_1}^{\alpha;I}|^4 + \sum_{\zeta_1,\zeta_2;\alpha,\beta;I} |C_{\zeta_1}^{\alpha;I}|^2 |C_{\zeta_2}^{\beta;I}|^2 \cos(\epsilon_{\zeta_1}^{\alpha;I} - \epsilon_{\zeta_2}^{\beta;I})t, \quad (9)$$

where the second term contains the separate contributions from each tunneling branch. The indices α, β indicate a particular number state group, ζ_i is the intrinsic index within each group and I denotes the respective energetical level. In particular, the first peak at frequency $\omega_1 \approx 3\Delta\omega$ (with $\Delta\omega = 2\pi/T$ and T denotes the propagation time) corresponds to the energy difference $\Delta\epsilon$ within the energetically lowest states of the single pair mode. Therefore the process corresponds to an intraband tunneling, e.g. from the state $|1, 2, 1\rangle_0$ to $|2, 1, 1\rangle_0$ etc. However, the second peak located at $\omega_2 \approx 125\Delta\omega$ refers to an interband transition between the states $|1, 2, 1\rangle_2$ and $|1, 2, 1\rangle_0$, which reflects the initial strongly correlated state. In the inset we present the δg -dependence of the location of the aforementioned peaks. As it can be seen the two branches are mainly steady as a function of the interaction quench, their frequencies are constrained in a narrow-band, while their amplitude (see main Figure) reduces significantly for weak quenches.

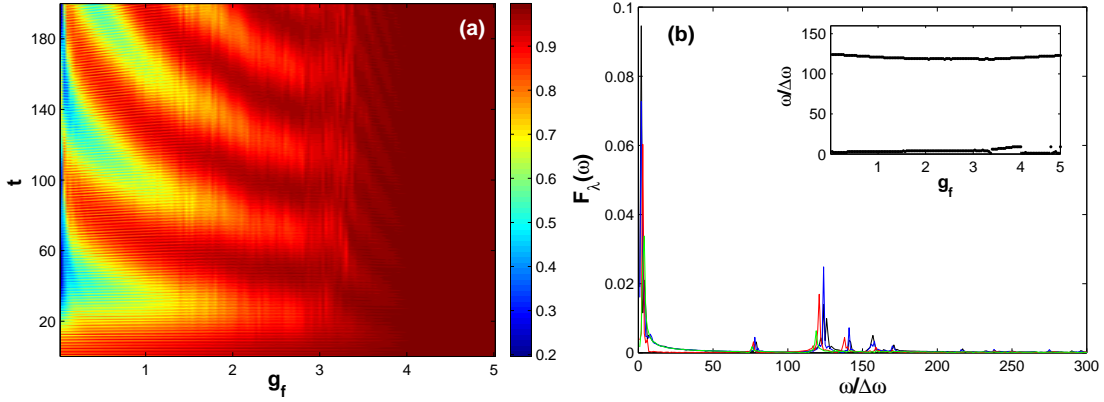


FIG. 3. (a) Fidelity evolution following negative interaction quenches for $g_{in} = 5.0$. (b) The frequency spectrum of the fidelity for $g_f = 0.1$ (black), $g_f = 0.6$ (blue), $g_f = 0.9$ (red) and $g_f = 1.8$ (green), which indicates the tunneling modes. The inset shows the dependence of each tunneling branch with respect to the final interaction strength after the quench. We incorporate 150 quenches in the range of $0 < g_f < 5.0$. The frequency units are normalized as $\omega/\Delta\omega$, with $\Delta\omega = 2\pi/T$ and T being the considered evolution time.

In the course of the investigation of the tunneling dynamics one fundamental question that has to be addressed is how correlations propagate [55] in the quenched system. In the present case, at

$t = 0$, a system of $N=4$ strongly interacting bosons ($g_{in} = 5.0$) is quenched to a weakly interacting state and we explore the response of the single particle correlations $C_{ij}(t) = \frac{1}{N} \langle \Psi | b_i^\dagger b_j | \Psi \rangle$. Here b_i^\dagger denotes the creation operator of a particle at the i -th well, while the diagonal elements $C_{ii}(t)$ correspond to the instantaneous density of the respective well. Figures 4(a)-(c) illustrate the time evolution for different components of the one-body correlations for various negative interaction quenches. We observe that the density oscillations C_{LL} of the left well are relatively weak for all quench amplitudes, while C_{MM} shows large amplitude oscillations for large quenches. C_{LL} and C_{MM} are anticorrelated with respect to their dynamics. We also observe an increase of the period T of the tunneling as we increase the interaction quench. The non-diagonal terms C_{ij} , $i \neq j$ exhibit a non-vanishing oscillatory behaviour with an amplitude much larger than the density oscillations. In particular, for increasing quench amplitude a substantial built-up of correlations between the left and right wells is observed. The above indicates an enhancement of the correlations between different sites as we increase the quench amplitude. Finally, notice that the single particle correlations oscillate even for long time scales which is due to the finite-size of our system.

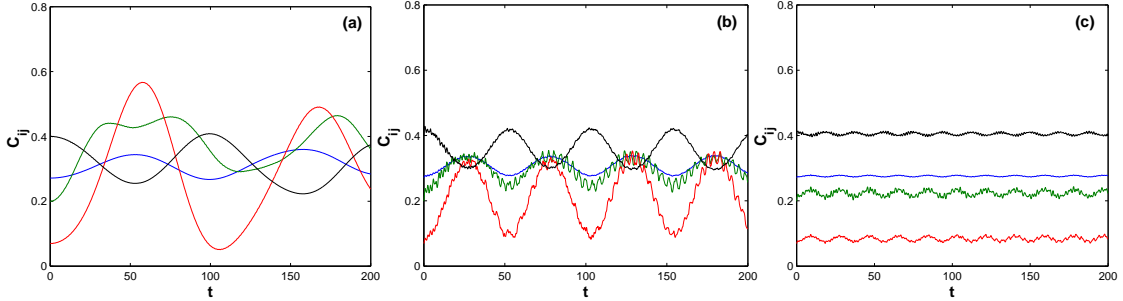


FIG. 4. The time evolution of the one-body correlation function C_{ij} after various negative interaction quenches for $g_{in} = 5.0$. Shown are different components of the correlation function C_{ij} with respect to the left well C_{LL} (blue line), C_{LM} (green line), C_{LR} (red line) and the middle well C_{MM} (black line) for final interactions (a) $g_f = 0.05$, (b) $g_f = 1.6$ and (c) $g_f = 3.8$.

3. The local breathing mode

The breathing mode can be used in order to measure some key quantities of a trapped system such as its kinetic and interaction energy or the coupling strength [28–30]. It refers to an expansion and contraction of the bosonic cloud and can be excited either via a variation of the interparticle interaction or a modulation of the frequency of the trapping potential.

In a similar manner, our quenched system exhibits local breathing oscillations which are most

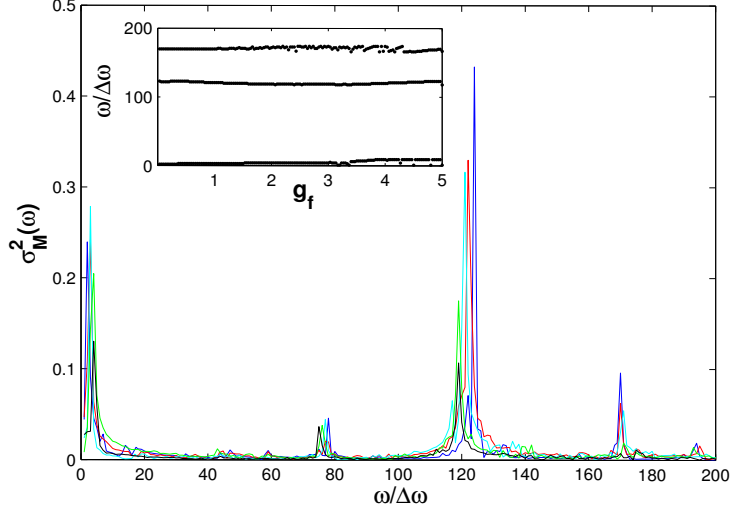


FIG. 5. Fourier spectrum of the second moment $\sigma_M^2(\omega)$ for the local breathing mode for different quench amplitudes. The initial state corresponds to $g_{in} = 5.0$ and the final interactions are $g_f = 0.15$ (blue), $g_f = 0.5$ (red), $g_f = 0.8$ (light-blue), $g_f = 1.7$ (light-green) and $g_f = 2.2$ (black). In the inset we show the δg -dependence of each breathing branch, where we incorporate 150 quenches in the range of $0 < g_f < 5.0$. Note that the frequency units are normalized with respect to $\omega/\Delta\omega$, where $\Delta\omega = 2\pi/T$ and T is the respective propagation time.

prominent in the subsystem corresponding to the middle well. This is illustrated from a one body perspective in Figure 2 where we observe a reshaping of the central well density during the propagation. To detect the frequencies of this normal mode we examine the variance of the coordinate of the center of mass for a particular well. The center of mass for the i -th well is defined as $X_{CM}^{(i)} = \int_{d_i}^{d'_i} dx (x - x_0^{(i)}) \rho_i(x) / \int_{d_i}^{d'_i} dx \rho_i(x)$. The index $i = R, M, L$ corresponds to the right, middle and left well respectively, while $x_0^{(i)}$ refers to the central point of the corresponding well. The limits of the wells are denoted by d_i and d'_i , whereas $\rho_i(x)$ is the respective single particle density (see eq.(2)). For the identification of the breathing process we define the operator of the second moment $\sigma_M^2(t) = \left\langle \left(x - X_{CM}^{(i)} \right)^2 \right\rangle$. The latter serves as a measure for the instantaneous spreading of the cloud in the i -th well and can also be used experimentally in order to probe the expansion velocity of a quenched condensate [27]. Then, if we connect the initial wavefunction with the eigenstates $|\zeta\rangle_{\alpha;I}$ of the final Hamiltonian H_f , we obtain

$$\begin{aligned} \sigma_M^2(t) = & \sum_{\alpha; \zeta_1; I} \left| C_{\zeta_1}^{\alpha; I} \right|^2_{\alpha; I} \langle \zeta_1 | \left(x - X_{CM}^{(i)} \right)^2 | \zeta_1 \rangle_{\alpha; I} + \\ & + 2 \sum_{\zeta_1 \neq \zeta_2} \text{Re} \left(C_{\zeta_1}^{\beta; I*} C_{\zeta_2}^{\alpha; I} \right)_{\beta; I} \langle \zeta_1 | \left(x - X_{CM}^{(i)} \right)^2 | \zeta_2 \rangle_{\alpha; I} \cos \left(\omega_{\zeta_1}^{\beta; I} - \omega_{\zeta_2}^{\alpha; I} \right) t. \end{aligned} \quad (10)$$

To identify the frequencies of the local breathing mode Figure 5 shows the frequency spectrum

of the second moment $\sigma_M^2(\omega) = \frac{1}{\pi} \int dt \sigma_M^2(t) e^{i\omega t}$, which refers to the middle well, for different quench amplitudes. Three main peaks can be observed. The lowest of these three peaks refers to a tunneling mode being identified from the energy difference within the energetically lowest states of the single pair mode. The appearance of this peak in the spectrum is due to the fact that the tunneling can induce a change in the width of the local wavepacket. The second and third peaks refer to interband processes and are related to higher-band transitions. In particular, the second peak is located at $\omega_2 \approx 125\Delta\omega$ and refers to a transition from $|1, 2, 1\rangle_0$ to $|1, 2, 1\rangle_2$, whereas the third one with frequency $\omega_3 \approx 170\Delta\omega$ corresponds to a transition from $|1, 2, 1\rangle_0$ to $|1, 2, 1\rangle_5$. To illustrate the dependence of the above three peaks on the interaction quench we show in the inset the evolution of the location of each peak with respect to the final interaction strength g_f after the quench. We observe that the branches are more sensitive for a quench to $2.0 < g_f < 4.0$, otherwise they are mainly constant.

The above discussion leads us to the conclusion that the breathing wavepacket for the middle well subsystem in the Fock space is given by

$$|\varphi\rangle_M^{br} = d_1(t)|1, 2, 1\rangle_0 + d_2(t)|1, 2, 1\rangle_2 + d_3(t)|1, 2, 1\rangle_5 \equiv |1, 2, 1\rangle_M^B, \quad (11)$$

where d_1 , d_2 , and d_3 denote the probability amplitudes of the respective Fock state.

4. The cradle mode

This mode refers to a dipole-like oscillation generated via an over-barrier transport due to the initially delocalized state between neighboring wells. In the present scenario it is induced by an interaction quench. From a one-body perspective the cradle mode is demonstrated by the inner well dynamics of the one-body density fluctuations $\delta\rho(x, t)$. Figure 6 shows the evolution of the system through the relative density after a sudden negative interaction quench from $g_{in} = 5.0$ to $g_f = 0.07$. The emergence of the cradle mode in the outer wells manifested as a dipole-like oscillation and the local breathing in the central well as a contraction and expansion dynamics is observed.

The initial spatial configuration due to the strong interparticle interaction corresponds to one localized boson in each well and one delocalized (over the three wells) energetically close to the barrier. In turn, the negative change in the interaction strength yields a high probability for the delocalized particle to overcome the barrier (over-barrier transport) and move to a neighboring well, where it performs a collision with the initially localized particle. This results in the cradle-like

mode inside the respective neighboring site and refers to a localized wave-packet oscillation. Note that the cradle is inherently related to the initial delocalization and after a negative interaction quench of a strongly correlated system can be excited only for incommensurate systems with filling factor $\nu > 1$. For other fillings it disappears and the consequent dynamics is dominated by the density-wave tunneling. Moreover, it stems from a two-body problem and posses two intrinsic frequencies that refer to the center of mass $\omega_C \equiv \omega$ and the relative frame $\omega_r \approx 2\omega$ of the harmonic potential approximation with effective frequency ω . It can be shown [36] that the wavefunction of the cradle mode for the center-of-mass motion at any time $t > 0$ is given by

$$\Psi(X_c; t) = \frac{1}{\sqrt{\sqrt{\pi}}} e^{-\frac{1}{2}(X_c - a \cos \omega t) - i(\frac{\omega t}{2} + X_c a \sin \omega t)}, \quad (12)$$

which represents a coherent state solution. Here, a refers to the relative distance of the two Gaussian wavepackets which form the cradle and $X_c = (x_1 + x_2) / \sqrt{2}$ to the center-of-mass coordinate of the harmonic potential approximation.

In the following, in order to quantitatively examine the inner-well dynamics we proceed with a local density analysis. For that purpose we divide a particular well from the center into two equal sections with $\rho_{a,1}(t)$ and $\rho_{a,2}(t)$ being the respective integrated densities of the left and right parts during the evolution. The index $a = L, M, R$ stands for the left, middle and right well respectively. In this manner, a measure of the intrawell asymmetry which captures the cradle motion is the quantity $\Delta\rho_a(t) = \rho_{a,1}(t) - \rho_{a,2}(t)$. Figure 7(a) shows the frequency spectrum of the above quantity for the left well, i.e. $\Delta\rho_L(\omega) = \frac{1}{\pi} \int dt \Delta\rho_L(t) e^{i\omega t}$ for various negative interaction quenches. From the spectrum we can identify two dominant peaks located at the positions $\omega_2 \approx 79\Delta\omega$ and $\omega_3 \approx 125\Delta\omega$. These two frequency branches correspond to the cradle mode. In addition, we observe a low-frequency peak related to the interwell tunneling at frequency $\omega_1 \approx 3\Delta\omega$. The inset shows the δg -dependence of the above three frequency peaks. The location of each branch remains essentially independent of the strength of the interaction quench and it is therefore constrained to a corresponding narrow-band.

To gain a deeper understanding of the cradle mode we again refer to a number state analysis and expand the initial state of the system in terms of the eigenstates of the final Hamiltonian as $|\Psi(0)\rangle = \sum_{\zeta; \alpha; I} C_{\zeta}^{\alpha; I} |\zeta\rangle_{\alpha; I}$. Then, the expectation value of the asymmetry operator reads

$$\begin{aligned} \langle \Psi | \Delta\hat{\rho}(t) | \Psi \rangle &= \sum_{\zeta_1; \alpha; I} \left| C_{\zeta_1}^{\alpha; I} \right|^2 {}_{I; \alpha} \langle \zeta_1 | \Delta\hat{\rho} | \zeta_1 \rangle_{\alpha; I} + \\ &+ 2 \sum_{\zeta_1 \neq \zeta_2} \text{Re} \left(C_{\zeta_1}^{\alpha; I*} C_{\zeta_2}^{\beta; I} \right) {}_{I; \alpha} \langle \zeta_1 | \Delta\hat{\rho} | \zeta_2 \rangle_{\beta; I} \cos \left[\left(\omega_{\zeta_1}^{\alpha; I} - \omega_{\zeta_2}^{\beta; I} \right) t \right]. \end{aligned} \quad (13)$$

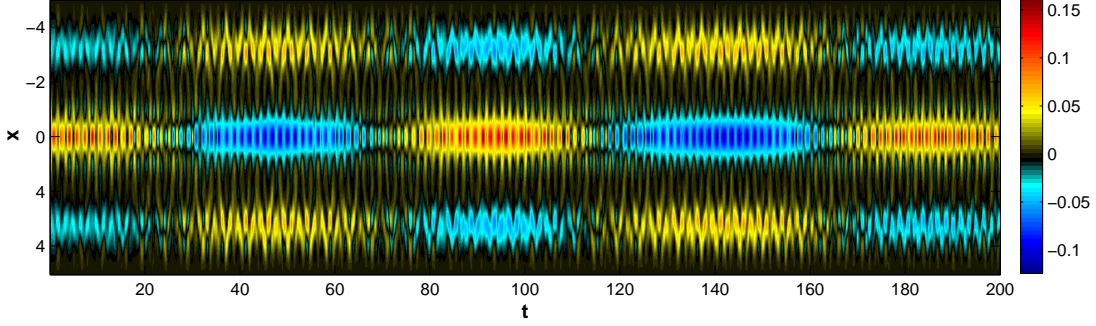


FIG. 6. Space-time evolution of the fluctuations $\delta\rho(x, t)$ after a sudden negative quench of the inter-particle repulsion from $g_{in} = 5.0$ to $g_f = 0.07$, thereby approaching the non-interacting limit. We observe the cradle mode in the left and right wells, the local breathing mode in the middle well and the density-wave tunneling during the evolution.

Here the terms of the second sum in the above expression which demonstrate an oscillatory behaviour describe the cradle mode. Therefore, we need to detect the eigenstates ($|\zeta\rangle_{\alpha;I}$) of the dominant oscillation terms, i.e. ${}_{\alpha;I}\langle\zeta|\Delta\widehat{\rho}|\zeta\rangle_{\beta;I} \neq 0$. A direct numerical analysis indicates that the respective eigenstates are $|\zeta\rangle_{1;0}$, $|\zeta\rangle_{1;1}$, $|\zeta\rangle_{1;2}$, whereas the corresponding significantly contributing number states are $|2, 1, 1\rangle_0$, $|2, 1, 1\rangle_1$ and $|2, 1, 1\rangle_4$ due to the fact that the corresponding oscillation frequency matches the energy difference between these eigenstates. Thus, one can infer that the minimal wavefunction which describes the cradle process in terms of Fock states for the left well (and similarly for the right) reads

$$|\varphi\rangle_L^{cr} = C_1(t)|2, 1, 1\rangle_0 + C_2(t)|2, 1, 1\rangle_1 + C_3(t)|2, 1, 1\rangle_4 \equiv |1, 2, 1\rangle_L^C, \quad (14)$$

where each coefficient C_i , $i = 1, 2, 3$ stands for the contribution of the respective number state in the course of the dynamics.

Let us now, investigate possible control protocols of the cradle mode via a modulation of its frequency by means of a varying potential parameter or via an external forcing. An efficient way to manipulate the frequency is to tune the height of the potential barriers. In this way, the cradle frequency can be reduced using a more shallow lattice (thereby making the excitation of the cradle mode more easy). Indeed, within the harmonic approximation it can be easily shown that the effective frequencies for two lattices with different potential depths $V_{0;1}$ and $V_{0;2}$, respectively, obey $\omega_{eff;1} = (V_{0;1}/V_{0;2})^{1/4}\omega_{eff;2}$. This situation is illustrated in Figure 7(b) where the frequency spectrum of the inner-well asymmetry with the same quench amplitude but different barrier heights $V_0 = 5.5$ (blue) and $V_0 = 3.5$ (red) is shown. We observe a negative shift of each frequency peak

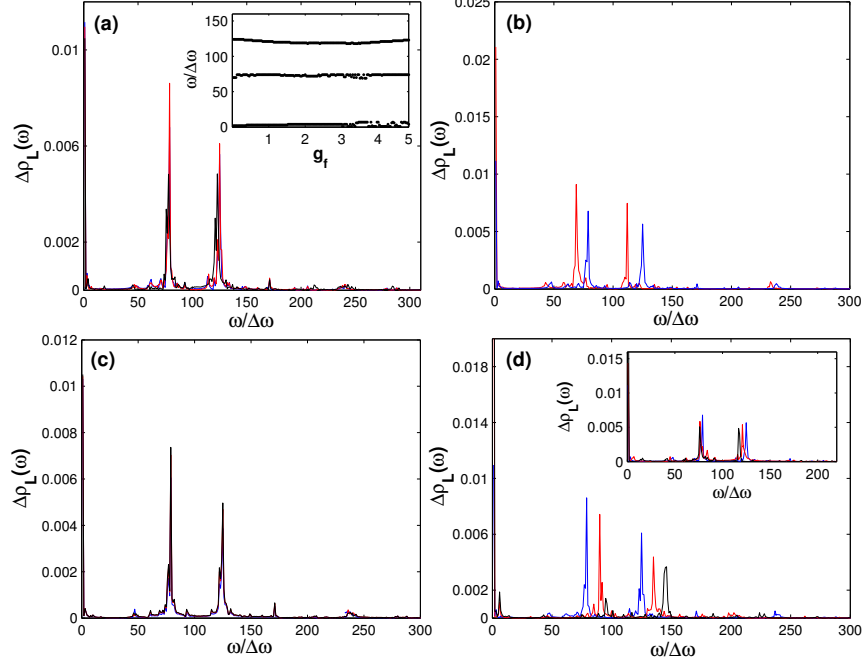


FIG. 7. The frequency spectrum of the intrawell asymmetry $\Delta\rho_L(\omega)$. (a) The final state of the system is obtained after a sudden negative interaction quench from $g_{in} = 5.0$ to $g_f = 0.05$ (blue), $g_f = 0.1$ (red) and $g_f = 0.45$ (black). The inset shows the evolution of each peak that refers to the cradle as a function of the quench amplitude (we incorporate 150 quenches in the range $0 < g_f < 5.0$). (b) The spectrum $\Delta\rho_L(\omega)$ for the same quench amplitude, $\delta g = -4.95$, and different barrier heights $V_0 = 5.5$ (blue) and $V_0 = 3.5$ (red). (c) Sudden quench to $g_f = 0.05$ starting from different initial conditions i.e. $g_{in} = 5.0$ (blue), $g_{in} = 4.0$ (red) and $g_{in} = 3.0$ (black). (d) Sudden quench to $g_f = 0.4$ and the hard-wall boundaries located at $x_\sigma = \pm 3\pi/2$ (blue), $x_\sigma = \pm 5\pi/4$ (red) and $x_\sigma = \pm 11\pi/8$ (black). In the inset we illustrate the spectrum of $\Delta\rho_L(\omega)$ for an imposed harmonic trap $V_{ext} = 0$ (blue), $V_{ext} = 0.02x^2$ (red) and $V_{ext} = 0.05x^2$ (black) on top of the lattice. Finally, note that in each case we use normalized frequency units $\omega/\Delta\omega$, with $\Delta\omega = 2\pi/T$ and T being the respective evolution time.

for a decreasing lattice depth which confirms our previous arguments. Alternatively, a similar manipulation of the cradle frequency can be achieved by comparing lattices with the same height of the potential barrier but different frequencies. Then, the respective effective frequencies are related via $\omega_{eff;1} = (l_2/l_1)^{1/2}\omega_{eff;2}$, where l is the distance between two successive potential minima.

Lets pose the question how the cradle mode frequency depends on g_{in} for fixed g_f . To answer this we illustrate in the inset of Figure 7(c) the frequency spectrum of the asymmetry operator where we start with a chosen initial strongly correlated state $g_{in} = 5.0$ (blue), $g_{in} = 4.0$ (red), $g_{in} = 3.0$ (black) and perform a sudden quench to the same final interaction $g_f = 0.05$. We observe

that the location of each peak remains essentially unchanged, indicating that the system does not keep any memory from the particular strongly correlated initial microscopic configuration.

A further question is to ask for the impact of the boundary conditions. Hence, we assume a fixed height for the barrier but changing the position of the hard wall boundary conditions. Then, we expect that as the wall is closer to the center of the right or left well the cradle would be more enhanced because effectively the frequency of the local harmonic oscillator is larger and so the period of the cradle reduces. Indeed, Figure 7(d) illustrates for the same quench amplitude the Fourier spectrum of the intrawell asymmetry $\Delta\rho_L(\omega)$ imposing the hard-wall boundaries at different positions, namely at $x_\sigma = \pm 3\pi/2$ (blue), $x_\sigma = \pm 5\pi/4$ (red) and $x_\sigma = \pm 11\pi/8$ (black). The frequency peaks of the cradle mode are shifted by a positive value for a closer to the center hard-wall. As a final attempt we impose a harmonic trap on top of the triple well, which increases the potential energy of the edge wells. Then the on-site energy of the Wannier states at the edges becomes larger than that (of the same degree of energetical excitation) in the central well. This in turn renders the initialization of the cradle mode more difficult, and for strong superimposed harmonic traps its excitation for a fixed quench amplitude becomes impossible. Accordingly, the inset of Figure 7(d) shows a scenario with the same quench amplitude but different superimposed harmonic traps $V_{\text{harm}} = 0.02x^2$ (red) and $V_{\text{harm}} = 0.05x^2$ (black). We observe negative variations and a reduction of the intensity of each peak for a stronger harmonic trap, thereby confirming our above discussion.

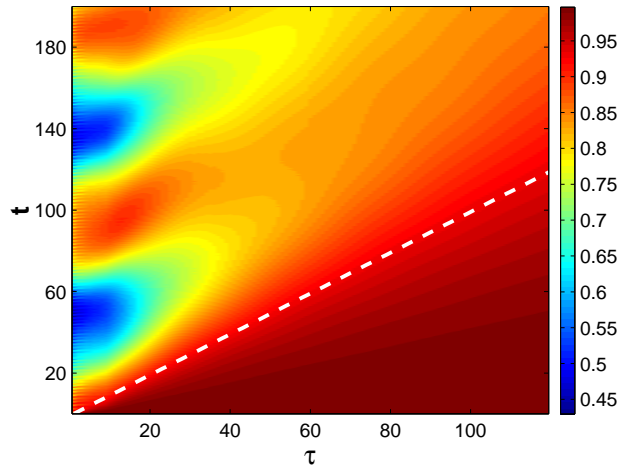


FIG. 8. Fidelity evolution for $g_{in} = 5.0$ and $g_f = 0.1$ as a function of the ramp-rate τ measured in units of the Heisenberg time τ_H (see text). The white dotted line correspond to the situation with $t = \tau$.

In the next subsection we explore the excitation modes induced by a time-dependent modulation

of the interaction strength and establish their presence also for this case.

5. Finite ramping

The present subsection is devoted to the study of the dynamics induced by time-dependent interaction quenches with a finite ramp-rate. In particular, we attempt to investigate quenches with the same amplitude but evolving on different time-scales, in order to gain a further insight into the dynamical response of the system with relevance to the experimentally occurring time-scales. To this end, let us adopt a time-dependent quench scenario of the form

$$g(t; \tau) = g_{in} + (g_f - g_{in}) \tanh(t/\tau). \quad (15)$$

Here g_{in} , g_f are the interaction strength for the initial and final state respectively, whereas τ denotes the finite ramp-rate of the performed quench. This protocol predicts the initial condition, i.e. $\lim_{t \rightarrow 0} g(t; \tau) = g_{in}$, while for very small ramp-rates it realizes the sudden quench scenario as $\lim_{\tau \rightarrow 0} g(t; \tau) = g_f$ and for large rates approaches the adiabatic limit, i.e. $\lim_{\tau \rightarrow +\infty} g(t; \tau) = g_{in}$. Focussing now on a strong non-equilibrium post-quench state with $g_f = 0.1$, Figure 8 shows the dynamical crossover, for finite evolution times, from an abrupt to an adiabatic interaction modulation for increasing ramp-rates τ . To interpret the resulting behaviour on a relevant time-scale we define the Heisenberg time $\tau_H \sim 1/\Delta\epsilon(\delta g)$, where $\Delta\epsilon(\delta g) = \epsilon(g_{in}) - \epsilon(g_f)$ refers to the energy difference between the ground state of the system before and after a sudden interaction quench. As it is shown for times $t < \tau$ (region under the white dotted line in Figure 8) the system essentially remains in the initial ground state of the unperturbed Hamiltonian. On the contrary, in the region with $t > \tau$, which spreads for decreasing τ (thereby approaching the sudden quench), the system starts to significantly depart from the initial state. Remarkably enough for $\tau < 30\tau_H$ we observe the appearance of blue lobes (overlap of the order of 40%) during the evolution which indicate the persistence of the excitation modes in this region. For $\tau > 30\tau_H$ we have a transition to a smoother dynamical departure of the system from the initial state and as a consequence the elimination of the excitation modes. In particular, for $\tau > 85\tau_H$ the Hamiltonian changes sufficiently slowly, i.e. the system tends to remain in the instantaneous ground state and therefore the modulation is almost adiabatic for the whole evolution time. For a smaller quench the adiabatic regime can be reached for sufficiently smaller time-scales due to the reduced impact of the quench to the system. These statements are also valid for a linear quench protocol of the form $g(t; \tau) = g_{in} + (g_f - g_{in})t/\tau$ for $t \leq \tau$, and $g(t; \tau) = g_f$ for $t > \tau$.

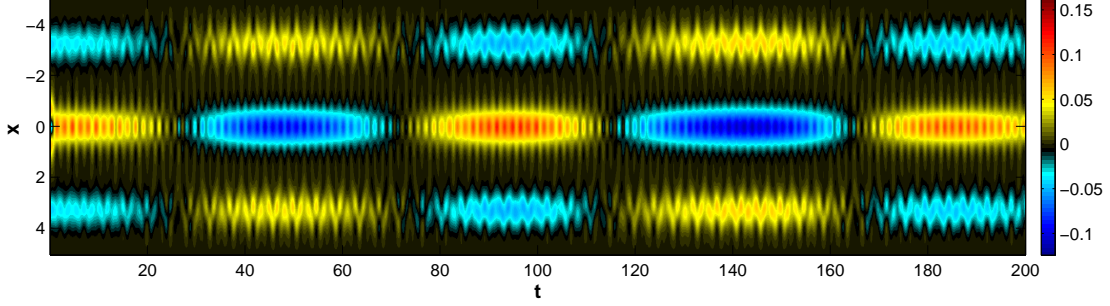


FIG. 9. The fluctuations $\delta\rho(x,t)$ of the one-body density caused by a negative time-dependent quench of the inter-particle repulsion to $g_f = 0.07$ ($g_{in} = 5.0$) with a finite ramp-rate $\tau = 0.8\tau_H$. For a direct comparison the quench parameters, here, have been chosen similar with Figure 6, which refers to the respective sudden quench scenario. We observe that the cradle mode in the left and right wells, the local breathing mode in the middle well and the density-wave tunneling during the evolution persist.

As a next step we study the effect of the time-dependent interaction quench on the excitation modes, i.e. the breathing and cradle processes. To give further insight in the overall non-equilibrium process Figure 9 illustrates the evolution of $\delta\rho(x,t)$, for the same relevant interactions as in Figure 6 where we considered a sudden quench, implementing now the time-dependent scenario of equation (15) with a finite rate $\tau = 0.8\tau_H$. The above-discussed modes still persist but with reduced intensity which is larger when the quench is faster.

According to this let us investigate how one can manipulate the local breathing mode via the quench rate τ . Figure 10 shows the frequency spectrum of the local breathing mode obtained for the same amplitude $\delta g = -4.9$ and different quench rates $\tau = 0\tau_H$ (black), $\tau = 0.8\tau_H$ (blue) and $\tau = 3.0\tau_H$ (red). As it can be seen the position of each peak remains the same but its intensity decreases significantly for larger rates. To further probe the position of each branch with respect to the quench rate τ we present in the inset the τ -dependence of each peak (without taking into account its intensity). It is obvious that each branch is quite insensitive to the interaction quench while in terms of its intensity (Figure 10), one can infer that by considering larger rates can gradually obliterate each frequency branch, i.e. for a faster quench the spectrum is more rich. Especially, one finds that for $\tau > 20\tau_H$ this mode can essentially be eliminated which means that the intensity of each peak is negligible (in our case $\leq 10^{-5}$).

Finally, we study the effect of the finite ramping on the cradle mode. Figure 10(b) presents the spectrum of the intrawell asymmetry $\Delta\rho_L(\omega)$ for an abrupt quench in the interparticle repulsion and two different quenches obeying the above time-dependent law with different rates τ but same

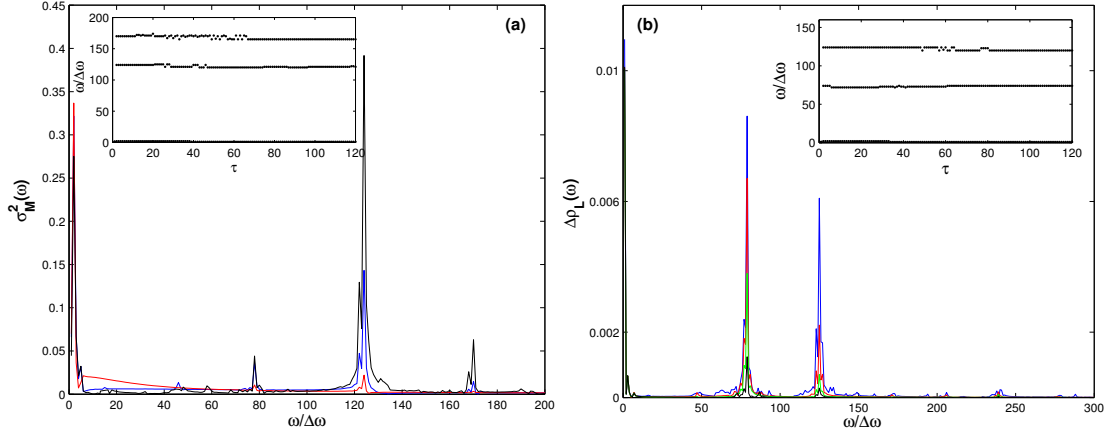


FIG. 10. The frequency spectrum for the variance of the middle well and the intrawell asymmetry $\Delta\rho_L(\omega)$ with respect to the left well. (a) Frequency spectrum of $\sigma_M^2(\omega)$ for time-dependent quenches of the form of equation (15) with final interaction $g_f = 0.1$ and rates $\tau = 0\tau_H$ (black), $\tau = 0.8\tau_H$ (blue) and $\tau = 3.0\tau_H$ (red). The inset shows each branch of the local breathing mode as a function of the quench rate τ (we incorporate 160 different rates in the range $0 < \tau < 120$). In (b) we present the spectrum of $\Delta\rho_L(\omega)$ for a time-dependent scenario with quench amplitude $\delta g = -4.90$ and rates $\tau = 0\tau_H$ (blue), $\tau = 0.8\tau_H$ (red), $\tau = 1.5\tau_H$ (light-green) and $\tau = 3.0\tau_H$ (black). The inset demonstrates the dependence of each branch of the cradle mode as a function of the quench rate τ . Finally, note that we have used normalized frequency units $\omega/\Delta\omega$, with $\Delta\omega = 2\pi/T$ and T being the respective evolution time.

final interaction as in the abrupt case. Moreover, in the inset we demonstrate the evolution of each peak (without taking into account its intensity) as a function of the ramp-rate τ . We observe that for larger rates τ the location of each frequency peak remains essentially the same (inset) but the respective amplitude tends to decrease, while for $\tau > 9.0\tau_H$ the third peak that refers to the second excited state in the left well has already been eliminated. Increasing further the rate $\tau > 30\tau_H$ one can eliminate the cradle (intensity $\leq 10^{-5}$) approaching the adiabatic region as also shown in Figure 8.

In the following section we turn to the study of the quench dynamics induced by a modulation of the optical lattice depth examining its dynamical response and the consequent excitation modes.

B. Quench of the optical potential depth for filling $\nu < 1$

Here we consider a quench protocol which consists of a ramp-down of the optical potential depth, thereby driving the system to a region where the kinetic energy of the atoms dominates in comparison to the potential energy. As we shall demonstrate, following this protocol one can

excite the cradle mode also for setups with filling $\nu < 1$. The system consists of five particles in an eight well setup but our conclusions can be easily generalized for arbitrary filling factors. To be self-consistent with the previous study we start from a strongly interacting initial state with $g_{in} = 5.0$, while the lattice is assumed to be initially deep enough with a depth $V_{0;in} = 8.0$ to include the first three Wannier energy levels. As usual, in order to interpret the dynamics induced by the quench we should be aware of the characteristics of the initial ground state. For a system with filling $\nu < 1$ the one-body density remains asymmetric even for strong interactions due to the low population, while the delocalized fraction of particles permits the presence of long range one particle correlations even in the strongly repulsive regime [56]. Only in the fermionization limit we observe a tendency to a phase with short-range correlations.

Let us firstly analyze the non-equilibrium dynamics induced by a sudden ramp-down of the optical potential depth at time $t=0$. The final Hamiltonian that governs the dynamics following the above scenario is given by

$$H_f(g, V_{0;f}) = H_0(g, V_{0;in}) + \frac{\delta V_0}{V_{0;in}} \sum_{k=1}^N V_{tr}(x_k), \quad (16)$$

with $V_{0;in}$, $V_{0;f}$ being the initial and final potential depth respectively, $\delta V_0 = V_{0;f} - V_{0;in} < 0$ due to the reduction of the barrier and V_{tr} being the lattice potential.

To examine the response of the system after the quench we initially rely on the fidelity $F_\lambda(t)$. We consider quenches of the barrier down to $V_{0;f} = 2.0$, where the lattice is quite shallow and includes only the first Wannier energy level while the others are considered as delocalized. Indeed, Figure 11(a) shows in a transparent way the instantaneous fidelity as a function of the final lattice depth. The rise of two different dynamical regions is observed. In the first region ($5.0 < V_{0;f} < 8.0$) the overlap is rather large with a minimum of the order of 80%, while in the second region ($2.0 < V_{0;f} < 5.0$) it can even reach 25% during the evolution. As we shall demonstrate below, the response of the system following this protocol is drastically different from that obtained through an interaction quench for fillings $\nu < 1$ where the dynamics is dominated by the density-wave tunneling. In particular, one can excite more on-site dynamical modes and even use a barrier quench on top of an interaction quench in order to excite the cradle mode. To indicate the latter and also to trigger more efficiently the dynamical modes from here on we mainly proceed by performing a simultaneous barrier and an interaction quench to weak interactions, i.e. $g_f = 0.02$. Figure 11(b) presents the fidelity during the dynamics induced by different quenches of the lattice depth and a simultaneous interaction quench to $g_f = 0.02$. The dynamical response of the system shows four different regions during the evolution. In the first (red part) the system is close to the initial state

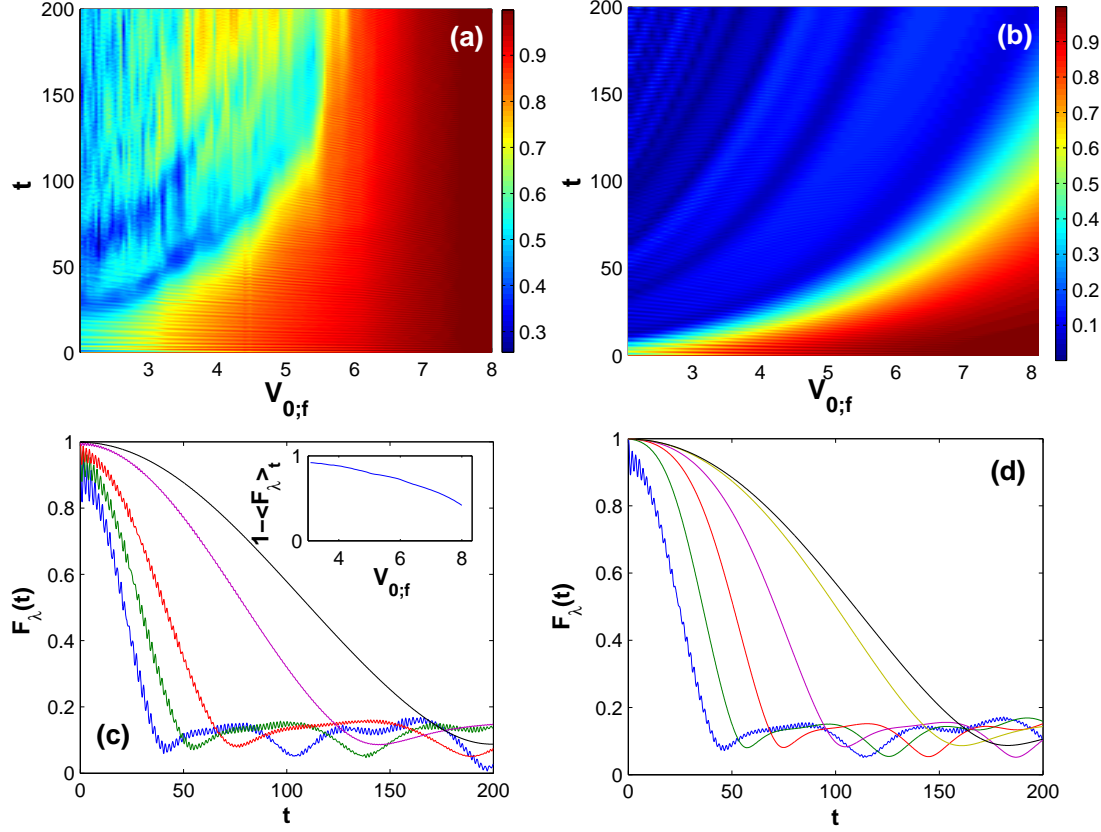


FIG. 11. (a) Fidelity evolution as a function of different sudden negative quenches of the optical lattice depth. The system consists of five strongly interacting bosons ($g = 5.0$) in an eight-well potential with $V_{0;in} = 8.0$. (b) Same but for different quenches of the lattice depth and a simultaneous interaction quench to $g_f = 0.02$. (c) Profiles of the fidelity evolution for different quench amplitudes $\delta V_0 = -3.8$ (blue), $\delta V_0 = -3.2$ (green), $\delta V_0 = -2.5$ (red), $\delta V_0 = -0.9$ (magenta), $\delta V_0 = -0.2$ (black) and a simultaneous interaction quench to $g_f = 0.02$. The inset shows the mean fidelity $1 - \langle F(t) \rangle_T$ with respect to the propagation period T versus the final lattice depth $V_{0,f}$. In (d) we present profiles of the fidelity following a negative time-dependent quench of the potential depth to $V_{0,f} = 4.0$ with different ramp-rates $\tau = 0.4\tau_H$ (blue), $\tau = 15.0\tau_H$ (green), $\tau = 40.0\tau_H$ (red), $\tau = 100.0\tau_H$ (magenta), $\tau = 400.0\tau_H$ (yellow) and $\tau = 800.0\tau_H$ (black) and a simultaneous interaction quench to $g_f = 0.02$.

with minimal percentage up to 80%, while the second (yellow-green) and the third (light-blue) regions indicate that the system significantly departs from the initial state with a percentage of the order of 50% and 30% respectively. The latter regions correspond to transition states following the combined quench. Finally, in the fourth section (blue) the system is driven to a completely different state possessing a maximal overlap of the order of 10%. In particular, for a fixed overlap a quadratic response of the system as a function of the quench amplitude is observed.

To analyze further the response of the system, Figure 11(c) illustrates some profiles of the fidelity in the course of the dynamics for different quenches. The fidelity exhibits a quadratic decay for short times, while after a characteristic time $\tau_c(\delta V_0)$ it oscillates around a constant value $F_0(\delta V_0)$, which depends on the quench amplitude such that it is larger for a smaller quench. The observed short-time quadratic behaviour can be easily explained as follows. Let $|\Psi_0\rangle$ be the initial eigenstate of H_0 , and $|\Psi(\delta t)\rangle$ the corresponding state after a short-time interval δt . Then, the short-time expansion of the overlap reads

$$|\langle\Psi_0|\Psi(\delta t)\rangle|^2 = 1 - (\delta t/\tau_c)^2 + \mathcal{O}((\delta t)^4), \quad (17)$$

where $\tau_c^{-1} = (\langle\Psi(\delta t)|H_f^2|\Psi(\delta t)\rangle - \langle\Psi(\delta t)|H_f|\Psi(\delta t)\rangle^2)^{1/2}$ is the quench characteristic time $\tau_c(\delta V_0)$ or so-called Zeno time [50, 57]. Especially, we observe that the time $\tau_c(\delta V_0)$ depends on the quench amplitude, i.e. for smaller quenches it becomes larger due to the smaller energy difference between the pre and post-quench states, and the system can not equilibrate fast. Furthermore, the rapid small amplitude oscillations during the decay are a consequence of the quantum interference and are predominantly due to the overbarrier transport induced by the quench. Thus, they are also a presignature of the cradle mode which is discussed below. The fact that at least some frequencies of the cradle mode could be indirectly observed in the fidelity spectrum is not surprising. Indeed, from the expansion of the fidelity (see eq.(9)) in terms of the number states it is obvious that when the contribution of the excited band states, that refer to the cradle, is significant the mode should also be observed in the fidelity spectrum. For smaller quenches these amplitude oscillations fade out, thereby indicating that the cradle is very weak. Finally, in order to gain further intuition for the overall mean sensitivity of the system after each quench we calculate the mean fidelity over the whole propagation time T , defined as $\langle F(t)\rangle_T = (1/T) \int_0^T dt F(t)$. The inset of Figure 11(c) presents $1 - \langle F(t)\rangle_T$ as a function of the final potential depth $V_{0,f}$ indicating again a mean quadratic response of the system with respect to the quench amplitude.

Furthermore, in order to unravel the crossover between a diabatic and an adiabatic quench, let us consider a time-dependent scenario of the form $V(t;\tau) = V_{0,in} + (V_{0,f} - V_{0,in}) \tanh(t/\tau)$. To obtain the physically relevant time-scales, let us rescale the physical time t by a dimensionless time, measured in units of the quench characteristic time scale τ_H . This scale can be estimated due to Heisenberg uncertainty principle as $\tau_H(\delta V_0) \sim 1/\Delta\epsilon(\delta V_0)$, where $\Delta\epsilon = \epsilon(V_{0,in}; g_{in}) - \epsilon(V_{0,f}; g_f)$ is the energy difference between the pre-quenched and the post-quenched system. Figure 11(d) demonstrates the fidelity in the course of the dynamics for an interaction quench to $g_f = 0.02$ and the same final potential depth $V_{0,f} = 4.4$ ($V_{in} = 8.0$) for different ramp rates τ . A direct

observation, here, is that the system has a similar quadratic response (for short-times) with respect to the quench, being accompanied by small amplitude oscillations especially for fast quenches, $\tau < 28\tau_H$. This indicates that the characteristics of the dynamics, such as the excitation modes, remain also for finite rates τ . By considering large rates τ the switch-on of the energy difference is sufficiently slow and an eigenstate of the initial Hamiltonian becomes approximately an eigenstate for the instantaneous final Hamiltonian. In this manner, we tend to approach the adiabatic limit and the system equilibrates in a slower manner while the small amplitude fast oscillations tend to disappear. Note that for smaller relative quench amplitudes the adiabatic limit is attained for smaller ramp-rates due to the reduced impact of the quench.

The reduction of the lattice depth allows for an initially delocalized boson to overcome the barrier if its kinetic energy dominates with respect to the potential energy. Then, it is possible to perform a collision with a second particle on the neighboring site and a cradle state can be generated. Figure 12 illustrates from the perspective of the relative density $\delta\rho(x, t)$ the evolution of the system after a negative change of the lattice depth from $V_{0,in} = 8.0$ to $V_{0,f} = 4.0$ and a simultaneous interaction quench from $g_{in} = 5.0$ to $g_f = 0.02$. The dynamics shows the propagation of inter-well density waves which reflect the dynamical tunneling via the population transport along the lattice, following the evolution of the bright regions. The corresponding propagation velocity is smaller for a smaller quench of the barrier. Furthermore, locally we observe the emergence of the cradle mode for the inner-well dynamics as a consequence of the overbarrier transport. However, this mode is hardly visible in Figure 12 due to the presented long evolution time and possesses a small amplitude as we shall demonstrate below.

The cradle mode refers to the inner-well oscillations between at least two bosons in the same well. The dominant number states for such a process exemplified using the first well are $|2, 0, 1, 1, 1, 0, \dots\rangle_0$ and $|2, 0, 1, 1, 1, 0, \dots\rangle_1$, with a straightforward extension for the remaining wells. To identify the presence of the cradle mode for the present setup we show in Figure 13 the intrawell asymmetry ($\Delta\rho_\alpha(t)$), for the second well of the lattice, as a function of time, and two different quench scenarios, i.e. an instantaneous ramp-down of the lattice depth (red curve) and its combination with a simultaneous interaction quench to $g_f = 0.02$ (blue curve). In the latter case the resulting amplitude is larger, which is due to the simultaneous interaction quench. For an incommensurate setup with filling $\nu > 1$ this amplitude is even more larger as the initially delocalized particles, energetically close to the barrier, render the system sensitive even to a small perturbation. We remark that by employing the time-dependent scheme one finds that for a quench to $V_{0,f} = 4.0$ with rate $\tau > 5\tau_H$ and a simultaneous sudden interaction quench to $g_f = 0.02$ the cradle mode is eliminated, while

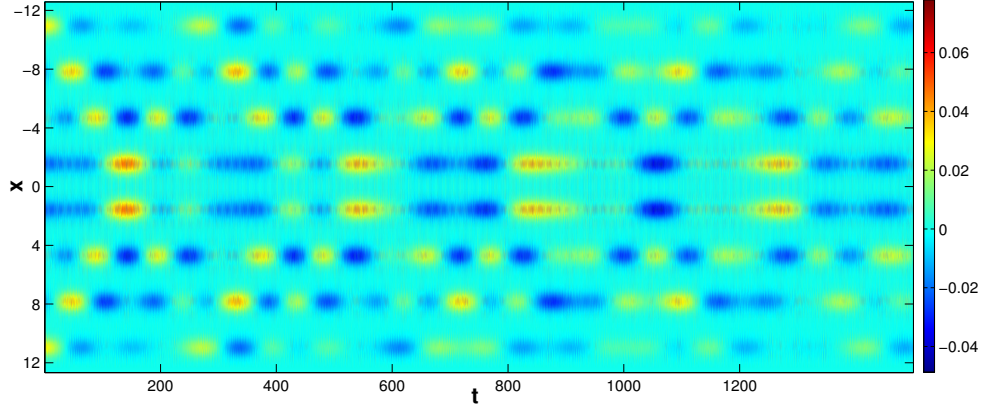


FIG. 12. The fluctuations $\delta\rho(x, t)$ of the one-body density caused by a sudden negative quench of the optical potential depth to $V_{0,f} = 4.0$ and a simultaneous interaction quench to $g_f = 0.02$. The initial state is the ground state of $N=5$ bosons confined in an eight-well setup with strong interparticle repulsion $g_{in} = 5.0$ and depth $V_{0,in} = 8.0$.

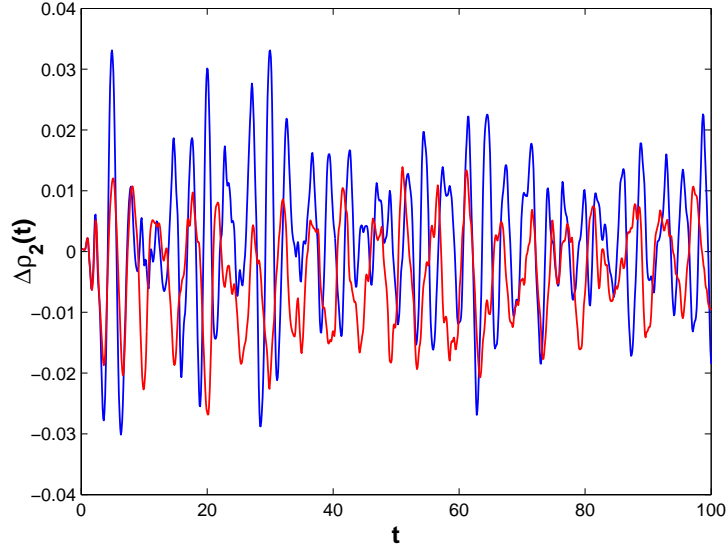


FIG. 13. The intrawell asymmetry $\Delta\rho_2(t)$ for the second well of the eight well setup for a barrier quench (red curve) to $V_{0,f} = 4.0$ and for the combined quench scenario i.e. barrier and interaction quench with final parameters $V_{0,f} = 4.0$ and $g_f = 0.02$ (blue curve).

the density-wave still persists up to $\tau = 40\tau_H$.

Finally, concerning the density wave tunneling in Figure 12 we note that it evolves on long time scales which can be attributed to the low-population. The consequent tunneling process can also be visualized from the evolution of the one-body reduced density matrix which essentially provides

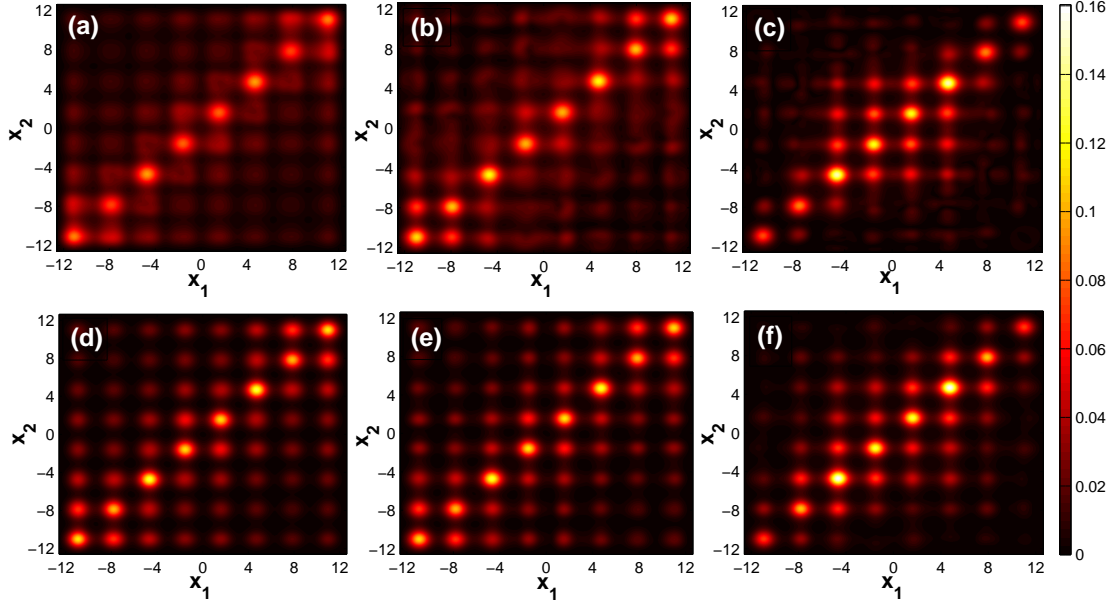


FIG. 14. The one-body reduced density matrix $\rho^{(1)}(x, x'; t)$ for five particles in eight wells for different time instants $t_1 = 68.0$ (a,d), $t_2 = 135.0$ (b,e) and $t_3 = 330.0$ (c,f) during the evolution. Shown are two values of the barrier quench with (a,b,c) $V_{0,f} = 3.8$ and (d,e,f) $V_{0,f} = 5.6$ performing also a simultaneous interaction quench to $g_f = 0.02$.

the elements of the one-body correlation function. Figure 14 depicts the function $\rho(x, x', t)$ for two different quenches of the height of the potential barrier, i.e. $V_{0,f} = 5.6$ and $V_{0,f} = 3.8$ and a simultaneous interaction quench to $g_f = 0.02$ at three different time instants $t_1 = 68$ (a,d), $t_2 = 135$ (b,e) and $t_3 = 330$ (c,f) of the propagation. Focussing on a specific quench the most prominent phenomenon is the alteration of the tunneling process as time evolves. This is indicated by the switch on and off concerning the off-diagonal elements. Here, one can also notice the large time-scales for the change in the tunneling process which is another sign of the evolution of the density-wave. Concerning the different quenches at the same time we observe that the smaller the reduction of the barrier is the more pronounced the long-range off-diagonal elements are. This indicates that the sudden ramp-down of the barrier induces a weak pinning and as a consequence a small suppression of the long-range correlations between different sites for larger quench amplitudes, while the short-range correlations remain almost unchanged.

IV. CONCLUSIONS AND OUTLOOK

We have investigated the quantum dynamics of strongly interacting bosons following a quench either to a weakly interacting final state or to a lattice with lowered barriers. The observed normal modes consist of the density-wave tunneling, a local breathing and a cradle mode. Each of these modes have been explained in detail, among others, within the concept of multiband Wannier number states which capture the population of excited states. The dominant Fock space for each mode has been identified showing the inclusion of higher-band contributions. Furthermore, a representative wavefunction in terms of number states has been provided for each particular mode. In this manner, conceptual differences concerning the ingredients of each mode as well as the corresponding excitation process in comparison with the case of positive interaction quenched [36] superfluids have been demonstrated.

The density-wave tunneling refers mainly to a direct population transport among the individual wells being manifested by the spatial oscillations in the one-body density during the dynamics. On the other hand, the local breathing mode refers to expansion and contraction dynamics of the bosons in an individual well. The cradle mode corresponds to a localized wavepacket oscillation and employing a harmonic approximation to a single well it can be described with a coherent state. For the interaction quench scenario where we start from a strongly interacting state and quench back to weak-interactions it is shown that the generation of the cradle mode is due to the initial delocalization. Therefore it can be observed only for setups with filling $\nu > 1$, while for the case of $\nu \leq 1$ it can be excited only with the aid of a barrier quench. This is a major difference in comparison to a positively interaction quenched superfluid where due to import of energy in the system we allow for the over-barrier transport independently of the filling factor. The fidelity function has been employed in order to investigate the response of the system and its long time evolution with respect to the quench amplitude, as well as to show the dynamical crossover from a sudden to an adiabatic parameter change. By considering time-dependent quenches, i.e. different quench rates, or the modulation of various potential parameters of the Hamiltonian we proposed scenarios to control the excited modes by manipulating their frequencies.

Our developed understanding of the excitation modes as well as the tunneling dynamics may pave the way to a control of the nonequilibrium dynamics of such strongly correlated systems. For instance, the finite ramp-rate of a time-dependent quench may allow for the control of the normal modes or the transport of a definite number of atoms. There are many ways to proceed in this direction. As an example we mention the non-equilibrium dynamics of mixtures of different bosonic

species in order to unravel their excitation modes or to create schemes for selective transport of an individual bosonic component.

APPENDIX: THE COMPUTATIONAL METHOD : ML-MCTDHB

Our analysis has been performed via the Multi-Layer Multi Configuration Time-Dependent Hartree method for Bosons (ML-MCTDHB) [38, 39] which constitutes an ab-initio method for the stationary properties but in particular the non-equilibrium quantum dynamics of bosonic systems. For a single species it is identical to MCTDHB which has been established [40, 41, 58] and applied extensively [58–61]. The multiconfigurational expansion of the wavefunction in MCTDH-type methods [62] takes into account higher-band effects which renders this approach unique for systems governed by temporally varying Hamiltonians, where the system can be excited to higher bands especially in the course of the dynamics. For instance, in our case the sudden or time-dependent change of a Hamiltonian parameter leads to higher-band excitations and as a consequence makes MCTDHB the appropriate tool for the study of the resulting non-equilibrium dynamics.

The advantage of the MCTDH-type methods in comparison to other exact computational methods is the representation of the wavefunction by a set of variationally optimal time-dependent orbitals. In turn, this implies the truncation of the total Hilbert space to an optimal one by employing a time-dependent moving basis in which the system can be instantaneously optimally represented by time-dependent Hartree products. The use of time-dependent orbitals is the key for the numerically exact treatment, i.e. we need a much smaller set of time-adaptive orbitals in order to achieve the same level of accuracy compared to the case of a static basis. To be self contained let us briefly introduce the basic concepts of the method and discuss how it can be adapted to our purposes.

The main underlying idea of the MCTDHB method is to solve the time-dependent Schrödinger equation $(i\hbar\partial_t - H)\Psi(x, t) = 0$ as an initial value problem. The expansion of the many-body wavefunction which is a linear combination of time-dependent permanents reads

$$|\Psi(t)\rangle = \sum_{\vec{n}} C_{\vec{n}}(t) |n_1, n_2, \dots, n_M; t\rangle, \quad (18)$$

where M is the number of orbitals and the summation is over all possible combinations which retain the total number of bosons. The permanents in terms of the creation operators $a_j^\dagger(t)$ for the j -th orbital $\varphi_j(t)$ are given by

$$|n_1, n_2, \dots, n_M; t\rangle = \frac{1}{\sqrt{n_1!n_2!\dots n_M!}} \left(a_1^\dagger\right)^{n_1} \left(a_2^\dagger\right)^{n_2} \dots \left(a_M^\dagger\right)^{n_M} |vac\rangle, \quad (19)$$

which satisfy the standard bosonic commutation relations $[a_i(t), a_j(t)] = \delta_{ij}$, etc. To proceed further, i.e. to determine the time-dependent wave function $|\Psi\rangle$ we have to find the equations of motion for the coefficients $C_{\vec{n}}(t)$ and the orbitals (which are both time-dependent). For that purpose one can employ various schemes such as the Lagrangian, McLachlan [63] or the Dirac-Frenkel [64, 65] variational principle. Following the Dirac-Frenkel variational principle $\langle \delta\Psi | i\partial_t - \hat{H} | \Psi \rangle = 0$ we can determine the time evolution of all the coefficients $C_{\vec{n}}(t)$ in the ansatz (18) and the time dependence for the orbitals $|\varphi_j\rangle$. In this manner, we end up with a set of M non-linear integrodifferential equations of motion for the orbitals which are coupled to the $\frac{(N+M-1)!}{N!(M-1)!}$ linear equations of motion for the coefficients. These equations are the well-known MCTDHB equations of motion [40, 41, 58, 66].

In terms of our implementation we have used a discrete variable representation for the orbitals and a sin-DVR which intrinsically introduces hard-wall boundaries at both ends of the potential (i.e. zero value of the wave function on the first and the last grid point). For the preparation of our initial state we rely on the so-called relaxation method in terms of which we can obtain the lowest eigenstates of the corresponding n -well setup. The key idea is to propagate some initial wave function $\Psi^{(0)}$ by the non-unitary $e^{-H\tau}$ (propagation in imaginary time). As $\tau \rightarrow \infty$, this exponentially damps out any contribution but that stemming from the ground state like $e^{-E_m\tau}$. In turn, we change either the initial interparticle interaction or the depth of the optical lattice abruptly or in a time-dependent manner in order to study the evolution of $\Psi(x_1, x_2, \dots, x_N; t)$ in the n -well potential within MCTDHB. Finally, note that in order to ensure the convergence of our simulations, e.g for the triple well, we have used up to 11 single particle functions thereby observing a systematic convergence of our results for sufficiently large spatial grids. Another criterion for ensuring convergence is the population of the lowest occupied natural orbital which is kept for each case below 0.1%.

ACKNOWLEDGMENTS

S.M. would like to thank P. Giannakeas, C. Morfonios and M. Mark for fruitful discussions and the Hamburgisches Gesetz zur Förderung des wissenschaftlichen und künstlerischen Nachwuchses (HmbNFG) for a PhD Scholarship. L.C. and P.S gratefully acknowledge funding by the Deutsche Forschungsgemeinschaft (DFG) in the framework of the SFB 925 Light induced dynamics and

control of correlated quantum systems.

- [1] I. Bloch, J. Dalibard, and W. Zwerger, *Rev. Mod. Phys.*, **80**(3), 885 (2008).
- [2] A. Polkovnikov, K. Sengupta, A. Silva, and M. Vengalattore, *Rev. Mod. Phys.*, **83**(3), 863 (2011).
- [3] M. Rigol, V. Dunjko, and M. Olshanii, *Nature*, **452**(7189), 854-858 (2008).
- [4] M. Olshanii, *Phys. Rev. Lett.*, **81**(5), 938 (1998).
- [5] R. Grimm, M. Weidemüller, and Y. B. Ovchinnikov, *Adv. At. Mol. Opt. Phys.*, **42**, 95-170 (2000).
- [6] R. A. Duine, and H. T. Stoof, *Phys. Rep.*, **396**(3), 115-195 (2004).
- [7] C. Chin, R. Grimm, P. Julienne, and E. Tiesinga, *Rev. Mod. Phys.*, **82**(2), 1225 (2010).
- [8] T. Müller, S. Fölling, A. Widera, and I. Bloch, *Phys. Rev. Lett.*, **99**(20), 200405 (2007).
- [9] G. Wirth, M. Ölschläger, and A. Hemmerich, *Nature Phys.*, **7**(2), 147-153 (2011).
- [10] S-P. Parvis, J. Struck, P. Hauke, A. Bick, W. Plenkers, G. Meineke, C. Becker, P. Windpassinger, M. Lewenstein, and K. Sengstock. *Nature Phys.*, **7**, no. 5 434-440 (2011).
- [11] W. S. Bakr, P. M. Preiss, M. E. Tai, R. Ma, J. Simon, and M. Greiner, *Nature*, **480** (7378), 500-503 (2011).
- [12] V. W. Scarola, E. Demler, and S. D. Sarma, *Phys. Rev. A*, **73**(5), 051601 (2006).
- [13] W. V. Liu, and C. Wu, *Phys. Rev. A*, **74**(1), 013607 (2006).
- [14] A. B. Kuklov, *Phys. Rev. Lett.*, **97**(11), 110405 (2006).
- [15] C. Wu, W. V. Liu, J. Moore, and S. D. Sarma, *Phys. Rev. Lett.*, **97**(19), 190406 (2006).
- [16] C. Wu, D. Bergman, L. Balents, and S. D. Sarma, *Phys. Rev. Lett.*, **99**(7), 070401 (2007).
- [17] M. Cheneau, P. Barmettler, D. Poletti, M. Endres, P. Schau, T. Fukuhara, C. Gross, I. Bloch, C. Kollath, and S. Kuhr, *Nature*, **481** no. 7382 484-487 (2012).
- [18] S.S. Natu, and E. J. Mueller, *Phys. Rev. A*, **87**(5), 053607 (2013).
- [19] E. Altman, and A. Auerbach, *Phys. Rev. Lett.*, **89**(25), 250404 (2002).
- [20] W. H. Zurek, U. Dorner, and P. Zoller, *Phys. Rev. Lett.*, **95**(10), 105701 (2005).
- [21] D. Chen, M. White, C. Borries, and B. DeMarco, *Phys. Rev. Lett.*, **106**(23), 235304 (2011).
- [22] H. Elmar, R. Hart, M. J. Mark, J. G. Danzl, L. Reichsöllner, M. Gustavsson, M. Dalmonte, G. Pupillo, and H.-C. Nägerl, *Nature*, **466** no. 7306: 597-600 (2010).
- [23] K. W. Mahmud, L. Jiang, P. R. Johnson, and E. Tiesinga, *New J. Phys.* **16** 103009 (2014).
- [24] S. Campbell, M. A. Garca-March, T. Fogarty, and T. Busch, *Phys. Rev. A* **90**, 013617 (2014).
- [25] M. Weidemüller, A. Hemmerich, A. Görlitz, T. Esslinger, and T. W. Hänsch, *Phys. Rev. Lett.*, **75**(25), 4583 (1995).
- [26] C. L. Hung, X. Zhang, L. C. Ha, S. K. Tung, N. Gemelke, and C. Chin, *New J. Phys.*, **13**(7), 075019 (2011).

- [27] J. P. Ronzheimer, M. Schreiber, S. Braun, S. S. Hodgman, S. Langer, I. P. McCulloch, F. Heidrich-Meisner, I. Bloch, and U. Schneider, *Phys. Rev. Lett.*, **110**(20), 205301 (2013).
- [28] J. W. Abraham, and M. Bonitz, *Contributions to Plasma Physics*, **54**(1), 27-99 (2014).
- [29] S. Bauch, K. Balzer, C. Henning, and M. Bonitz, *Phys. Rev. B*, **80**(5), 054515 (2009).
- [30] S. Bauch, D. Hochstuhl, K. Balzer, and M. Bonitz, In *Journal of Physics: Conference Series* (Vol. **220**, No. 1, p. 012013). IOP Publishing (2010).
- [31] J. W. Abraham, K. Balzer, D. Hochstuhl, and M. Bonitz, *Phys. Rev. B*, **86**(12), 125112 (2012).
- [32] R. Schmitz, S. Krönke, L. Cao, and P. Schmelcher, *Phys. Rev. A*, **88**(4), 043601 (2013).
- [33] S. Peotta, D. Rossini, M. Polini, F. Minardi, and R. Fazio, *Phys. Rev. Lett.*, **110**(1), 015302 (2013).
- [34] W. Kohn, *Phys. Rev.* **123**, 1242 (1961).
- [35] M. Bonitz, K. Balzer, and R. Van Leeuwen, *Phys. Rev. B*, **76**(4), 045341 (2007).
- [36] S. I. Mistakidis, L. Cao, and P. Schmelcher, *J. Phys. B: At. Mol. Opt. Phys.* **47** 225303 (2014).
- [37] P. Makotyn, C. E. Klauss, D. L. Goldberger, E. A. Cornell, and D. S. Jin, *Nature Phys.*, (2014).
- [38] L. Cao, S. Krönke, O. Vendrell, and P. Schmelcher, *J. Chem. Phys.*, **139**(13), 134103 (2013).
- [39] S. Krönke, L. Cao, O. Vendrell, and P. Schmelcher, *New J. Phys.*, **15**(6), 063018 (2013).
- [40] O. E. Alon, A. I. Streltsov, and L. S. Cederbaum, *J. Chem. Phys.*, **127**, 154103 (2007).
- [41] O. E. Alon, A. I. Streltsov, and L. S. Cederbaum, *Phys. Rev. A*, **77**(3), 033613 (2008).
- [42] J. I. Kim, V. S. Melezhik, and P. Schmelcher, *Phys. Rev. Lett.*, **97**(19), 193203 (2006).
- [43] T. Bergeman, M. G. Moore, and M. Olshanii, *Phys. Rev. Lett.*, **91**(16), 163201 (2003).
- [44] P. Giannakeas, F. K. Diakonov, and P. Schmelcher, *Phys. Rev. A*, **86**(4), 042703 (2012).
- [45] P. A. Martin, and F. Rothen, *Many-body problems and quantum field theory: an introduction*. Springer (2004).
- [46] R. W. Spekkens, and J. E. Sipe, *Phys. Rev. A*, **59**(5), 3868 (1999).
- [47] S. Klaiman, N. Moiseyev, and L. S. Cederbaum, *Phys. Rev. A*, **73**(1), 013622 (2006).
- [48] E. J. Mueller, T. L. Ho, M. Ueda, and G. Baym, *Phys. Rev. A*, **74**(3), 33612 (2006).
- [49] O. Penrose, and L. Onsager, *Phys. Rev.*, **104**(3), 576 (1956).
- [50] T. Gorin, T. Prosen, T. H. Seligman, and M. Žnidarič, *Phys. Rep.*, **435**(2), 33-156 (2006).
- [51] M. P. Fisher, P. B. Weichman, G. Grinstein, and D. S. Fisher, *Phys. Rev. B*, **40**(1), 546 (1989).
- [52] J. K. Freericks, and H. Monien, *EPL*, **26**(7), 545 (1994).
- [53] J. K. Freericks, and H. Monien, *Phys. Rev. B*, **53**(5), 2691 (1996).
- [54] K. Sakmann, A. I. Streltsov, O. E. Alon, and L. S. Cederbaum, *Phys. Rev. A*, **89**(2), 23602 (2014).
- [55] S. Bravyi, M. B. Hastings, and F. Verstraete, *Phys. Rev. Lett.*, **97**(5), 050401 (2006).
- [56] I. Brouzos, S. Zöllner, and P. Schmelcher, *Phys. Rev. A*, **81**(5), 053613 (2010).
- [57] A. Peres, *Am. J. Phys.*, **48**, 913 (1980).
- [58] A. I. Streltsov, O. E. Alon, and L. S. Cederbaum, *Phys. Rev. Lett.*, **99**(3), 030402 (2007).
- [59] A. I. Streltsov, K. Sakmann, O. E. Alon, and L. S. Cederbaum, *Phys. Rev. A*, **83**(4), 043604 (2011).
- [60] O. E. Alon, A. I. Streltsov, and L. S. Cederbaum, *Phys. Rev. A*, **76**(1), 013611 (2007).

- [61] O. E. Alon, A. I. Streltsov, and L. S. Cederbaum, Phys. Rev. A, **79**(2), 022503 (2009).
- [62] M. H. Beck, A. Jäckle, G. A. Worth, and H. D. Meyer, Phys. Rep., **324** (1999).
- [63] A. D. McLachlan, Mol. Phys., **8**(1), 39-44 (1964).
- [64] J. Frenkel, Wave mechanics, (pp. 423-28). Oxford (1934).
- [65] P. A. Dirac, (1930, July). Proc. Camb. Phil. Soc. (Vol. **26**, No. 03, pp. 376-385). Cambridge University Press.
- [66] J. Broeckhove, L. Lathouwers, E. Kesteloot, and Van Leuven, P. Chem. Phys. Lett., **149**(5), 547-550 (1988).